LUND UNIVERSITY

Advanced Optical Diagnostics in Particle Combustion for Biomass and Metal as Alternative Fuels

Li, Shen

2022

[Link to publication](#)

Citation for published version (APA):
Li, S. (2022). *Advanced Optical Diagnostics in Particle Combustion for Biomass and Metal as Alternative Fuels*. Department of Combustion Physics, Lund University.

Total number of authors:
1

Advanced Optical Diagnostics in Particle Combustion for Biomass and Metal as Alternative Fuels

SHEN LI
DIVISION OF COMBUSTION PHYSICS | FACULTY OF ENGINEERING | LUND UNIVERSITY

Advanced Optical Diagnostics in Particle Combustion for Biomass and Metal as Alternative Fuels

Advanced Optical Diagnostics in Particle Combustion for Biomass and Metal as Alternative Fuels

Shen Li

LUND
UNIVERSITY

DOCTORAL DISSERTATION
by due permission of the Faculty of Engineering, Lund University, Sweden.
To be defended at Rydbergssalen, Professorsgatan 1, Lund. Date 23rd Sept.
2022, at 09:15.

Faculty opponent
Prof. Jeffery Bergthorson
Mechanical Engineering Department, McGill University, Montreal, Canada

Organization		Document name	
Organization LUND UNIVERSITY		**Document name** DOCTORAL DISSERTATION	
Division of Combustion Physics Department of Physics PO Box 118, SE-221 00 LUND, Sweden		**Date of issue** 2022-08-30	
Author(s) Shen Li		Sponsoring organization	

Title and subtitle
Advanced Optical Diagnostics in Particle Combustion for Biomass and Metal as Alternative Fuels

Abstract

The energy sector is in urgent need for carbon-free strategies considering environmental pollutions and climate change impact. Two kinds of solid fuels, biomass and metal particles have been studied in this thesis aiming at CO_2 emission reduction or zero carbon emission.

Biomass is a renewable and carbon-neutral energy source that provides heat and power through gasification and combustion. Biomass fuels usually contain varying amounts of potassium, which will cause severe operational problems, such as slagging and corrosion by the potassium released during thermal conversion processes. The detailed potassium chemistry in biomass thermochemical conversion processes has been investigated in our previous study and presented in Weng's doctoral dissertation. Based on these quantitative studies, the work presented in this thesis is mainly focused on the quantitative measurement of burning a single biomass pellet and the potassium released from burning pulverized biomass char particles. The motivation for the study of biomass char particles is that over 80% of the potassium can remain in the char particles from the raw biomass.

Laser-induced photofragmentation fluorescence (LIPF) imaging was adopted here to measure the potassium release process for biomass char particles, which provides spatially resolved information of the dominant species of KCl and KOH that formed during the char oxidation period. A hot laminar gas flow was used for calibration with gas-phase KOH and KCl provided by a homemade multi-jet burner, in which a homogenous temperatures distribution ranging from 1000 to 2000 K are provided. Newly developed UV-absorption spectroscopy was adopted to monitor the concentrations of KOH and KCl. Based on the calibration, the KOH/KCl distribution surrounding the burning char particles was derived, revealing the potassium release process during the char oxidation period.

Metal fuels have been used as sustainable energy carriers due to their zero-carbon emission and high energy density. The iron powder has been proposed as one of the most promising recyclable metal fuels for the future low-carbon society. A comprehensive understanding of the combustion behavior of iron particles is essential for investigating fundamental mechanisms and designing efficient iron powder combustors. A versatile metal powder seeding apparatus has been designed and optimized based on electrostatic dispersion. This dispersion system is well calibrated for powder concentration that can provide a stable flow of particles seeding for nearly one minute.

The work presented in this thesis mainly focuses on investigating single iron particle combustion in a well-controlled laminar premixed flame with a modified Mckenna flat-flame burner through advanced optical diagnostic techniques. One of the challenges for the study of metal combustion came from the small size (~20 to 80 μm) of the metal particles and their movement in the hot combustion environment. This work, inspired by clustering algorithms, proposed a new clustering-based particle detection (CBPD) method for digital holography (DH) for particle detection. This data-driven method features automatic recognition of particles, particle edges and background, and accurate separation of overlapping particles. Based on CBPD method, high-speed digital in-line holography (DIH), a three-dimensional (3D) imaging technique, is employed to reconstruct the 3D particle field and simultaneously quantify the size, 3D location and velocity of burning iron particles in a well-controlled $CH_4/N_2/O_2$ premixed Bunsen flame with a stable metal power seeded.

The ignition delay time, combustion time of single micron-sized iron particles are studied by high-speed imaging in different flame conditions. Particle temperatures are measured by an ICCD camera equipped with a stereoscopy, and the results are derived through the two-color pyrometry method. An important phenomenon of nano-sized iron-oxides particles releasing during the iron particles combustion has been identified. Micro-explosion of burning iron particles was observed during the combustion process, which is complex and can affect combustion stability and the formation of product components. The morphology of raw iron particles and the combust products (iron oxides) collected by sampling meshes have been analyzed by scanning electron microscopy (SEM).

Key words: Optical diagnostics, Quantitative measurement, Iron powder, Biomass, High-speed imaging, Digital holography 3D reconstruction, SEM

Classification system and/or index terms (if any)

Supplementary bibliographical information		**Language: English**
ISSN and key title 1102-8718		**ISBN** 978-91-8039-358-4 (print) 978-91-8039-357-7 (pdf)
Recipient's notes	**Number of pages** 231	Price
	Security classification	

I, the undersigned, being the copyright owner of the abstract of the above-mentioned dissertation, hereby grant to all reference sources permission to publish and disseminate the abstract of the above-mentioned dissertation.

Signature *shen li* Date 2022-08-15

Advanced Optical Diagnostics in Particle Combustion for Biomass and Metal as Alternative Fuels

Shen Li

LUND
UNIVERSITY

Faculty of Engineering, Department of Physics

Division of Combustion Physics

To my beloved families

To the braved past-self, to the braver future-self

Table of Contents

Abstract

The energy sector is in urgent need for carbon-free strategies considering environmental and climate change impact. Two kinds of solid fuels, biomass and metal particles have been studied in this thesis aiming at CO_2 neutral and zero carbon emission.

Biomass as a renewable and carbon-neutral energy source, can be used to provide heat and power through gasification and combustion. Biomass fuels usually contain large amounts of potassium, which will cause severe operational problems, such as slagging and corrosion by the released potassium during thermal conversion processes. The work presented in this thesis is mainly focused on in-situ quantitative measurements of potassium released from burning single biomass pellets and pulverized biomass char particles. The motivation for the study of biomass char particles is that over 80% of the potassium can remain in the char particles.

Laser-induced photofragmentation fluorescence (LIPF) imaging was adopted to measure the potassium release process for biomass char particles, which provides spatially resolved information of the dominant species KCl and KOH that were formed during the char oxidation period. A hot laminar gas flow with gas-phase KOH and KCl provided by a multi-jet burner was used for calibration. A homogenous temperature distribution ranging from 1000 to 2000 K was covered. UV-absorption spectroscopy was adopted to monitor the concentrations of KOH and KCl. Based on the calibration, the KOH/KCl distribution surrounding the burning char particles was derived.

Metal fuels have been suggested as sustainable energy carriers due to their zero-carbon footprint and high energy density. Iron powder has been proposed as one of the most promising recyclable metal fuels for the future low-carbon society. A comprehensive understanding of the combustion behavior of iron particles is essential for the designing of efficient iron powder combustors. A versatile metal powder seeding apparatus has been designed and optimized based on electrostatic dispersion. This dispersion system is well calibrated for powder concentration that can provide a stable flow of metal particles seeding.

The work presented in this thesis mainly focuses on investigating single iron particle combustion in a well-controlled laminar premixed flame with a modified Mckenna flat-flame burner through advanced optical diagnostic techniques. One of the challenges for the study of metal combustion came from the small size (~20 to 80 µm) of the metal particles and their movement in the hot combustion environment.

In this work, a clustering-based particle detection (CBPD) method was developed for digital holography (DH) particle detection. This data-driven method features automatic recognition of particles, particle edges from the background, and accurate separation of overlapping particles. Based on the CBPD method, high-speed digital

in-line holography (DIH), a three-dimensional (3D) imaging technique, is employed to reconstruct the 3D particle field and simultaneously quantify the size, 3D location and velocity of burning iron particles in a well-controlled $CH_4/N_2/O_2$ premixed flame with a stable metal power seeding.

The ignition delay and combustion time of burning micron-sized iron particles are studied by high-speed imaging in different flame conditions. Particle surface temperatures are measured using thermal emission by an ICCD camera equipped with a stereoscope, and the results are derived through a two-color pyrometry method. An important phenomenon of nano-sized iron-oxides particles released during the iron particles combustion has been identified. Micro-explosions of burning iron particles were observed during the combustion process, which can affect combustion stability and the formation of product components. The morphology of raw iron particles and the combustion products (iron oxides) collected by sampling meshes have been analyzed by scanning electron microscopy (SEM).

Popular science

In the global energy system, fossil fuels have been predominated as the primary energy for centuries. Fossil fuel consumption will result in severe air pollution and global climate changes. Recently, clean energy technologies have been developed rapidly and can potentially eliminate fossil fuels. Thus, increasing the share of the renewable and carbon-neutral proportion in the total energy consumption is a trend, including biomass fuel, wind, solar, and hydro energy. Alternative fuel utilization is continually increasing in the global energy consumption aiming at CO_2 emission reduction.

Biomass fuel is renewable organic material that comes from plants, mainly produced from forest and agriculture residues. Many biomass fuels contain high amounts of potassium, which can be released in different thermal conversion processes. The potassium release increases the risk of slagging and corrosion in combustion equipment. One focus of this thesis is to study the release of potassium in biomass gasification and combustion to help to increase the efficiency of utilization of biomass fuel and lower emissions.

According to the Paris climate deal, the EU aims to cut greenhouse gases emissions by 55% by 2030 compared to 1990 levels. More than 40% of the global CO_2 emissions come from heat-generating, electrical-consuming industries, flights, and the maritime transport sector. However, these industries cannot completely fulfill the zero-carbon emissions targets due to the existing carbon-free energy alternatives, which cannot offer an efficient and low-cost solution to every application and meet process requirements simultaneously. Among the handful of solutions such as batteries, solar, hydrocarbon fuels, metal fuels as promising energy carriers due to their high energy densities and zero-carbon emission, yet largely overlooked.

It is required to have a deep understanding and control of the combustion process of these metal particles in order to utilize these metals as fuels. In this thesis, a seeding apparatus for supplying a small and stable metal particle flow using electrostatic dispersion has been designed and optimized. It is important for further study and investigation of combustion characteristics of metal particles. We focused on the single micron-sized iron particles combustion since the properties of individual burning iron particles play an essential role in the characteristic of iron dust flame. The iron dust flame consists of single burning iron particles where intensive oxidation/reaction happens during the heterogeneous combustion of iron powders. The burning time and particle temperature of single particle combustion, which depend on the particle size and oxygen concentration in the hot gas flow, were experimentally investigated based on optical diagnostics.

During the combustion of micron-sized iron powder, a nanoparticles release phenomenon was observed in the iron particle combustion using magnified thermal radiation imaging and high-speed shadowgraphy. This release was mainly

composed of iron nanoparticles and was indirectly confirmed by the scanning electron microscopy of the combustion products, revealing multiple cracked particle shells and hollow structures. The formed nanoparticles are hard to collect and recycle to fulfill the metal fuel loop, which should be avoided during burning the iron particles. In certain flame conditions, especially for burning the iron particle in the diffusive flame, it is common to observe the micro-explosion of the burning iron particles. Some burning iron particles terminate with a micro-explosion rather than a gradual burnout. These particles broke up into smaller fragments that burned out quickly. This kind of explosion in the combustion process is generally manifested as the nonlinear change of iron powder trajectory and the formation of smaller fragments. The micro-explosions will dramatically affect the key combustion characteristics of the particles. A comprehensive understanding of the mechanism of micro-explosion is presented to control the micro-explosion during iron particle combustion for practical applications.

List of papers

I.   **S. Li**, W. Weng, C. Kong, M. Aldén, Z. Li. *Dual-laser-induced Breakdown Thermometry via Sound Speed Measurement: A New Procedure for Improved Spatiotemporal Resolution*, **Sensors** 20 (2020) 2803.

II.   W. Weng, H. Feuk, **S. Li**, M. Richter, M. Aldén, Z. Li, *Temporal temperature measurement on burning biomass pellets using phosphor thermometry and two-line atomic fluorescence*, **Proceedings of the Combustion Institute** 38 (2021) 3929-3938.

III.   W. Weng, **S. Li**, M. Costa, and Z. Li. *Quantitative imaging of potassium release from single burning pulverized biomass char particles*, **Fuel** 264 (2020) 116866.

IV.   W. Weng, **S. Li**, M. Costa, Z. Li, *Particle temperature and potassium release during combustion of single pulverized biomass char particles*, **Proceedings of the Combustion Institute** 38 (2021) 3949-3958.

V.   J. Huang, **S. Li**, Y. Zi, Y. Qian, W. Cai, M. Aldén, Z. Li, *Clustering-based particle detection method for digital holography to detect the three-dimensional location and in-plane size of particles*, **Measurement Science and Technology** 32 (2021) 055205.

VI.   J. Huang[†], **S. Li**[†], W. Cai, Y. Qian, E. Berrocal, M. Aldén, Z. Li, Quantification of the size. *3D location and velocity of burning iron particles in premixed methane flames using high-speed digital in-line holography*, **Combustion and Flame** 230 (2021) 111430.

VII.   **S. Li**, W. Weng, Y. Qian, M. Aldén, Z. Li, *A versatile metal powder burner for quantitative optical diagnostics of single burning particles and percolation flames*. **In manuscript**.

VIII.   **S. Li**, J. Huang, W. Weng, Y. Qian, X. Lu, M. Aldén, Z. Li, *Ignition and combustion behavior of single micro-sized iron particle in hot gas flow*, **Combustion and Flame** 241 (2022) 112099.

IX.   J. Huang[†], **S. Li**[†], D. Sanned, L. Xu, S. Xu, Y. Qian, Q. Wang, M. Stiti, W. Cai, E. Berrocal, M. Aldén, M. Richter, Z. Li. *A detailed study on the micro-explosion of burning iron particles in hot oxidizing environments*. **Combustion and Flame** 235 (2022) 11755.

X. **S. Li**, D. Sanned, J. Huang, E. Berrocal, W. Cai, M. Aldén, M. Richter, Z. Li. *Stereo High-Speed imaging of iron particles micro-explosions and nanoparticles-release*, **Optics Express**, 21 (2021) 34465-34476.

XI. S. Xu, Y. Qiu, L. Xu, J. Huang, **S. Li**, E.J.K. Nilsson, Z. Li, M. Aldén, X-S Bai. *Phase change and combustion of iron particles in premixed $CH_4/O_2/N_2$ flames*, **Submitted to Combustion and Flame**.

Related work

Papers not included in this thesis:

A. W. Weng, **S. Li**, M. Aldén, and Z. Li. *Ultraviolet Absorption Cross Sections of NH_3 at Elevated Temperatures for Nonintrusive Quantitative Detection of Ammonia in Combustion Environments,* **Applied Spectroscopy**. 9 (2021) 1168-1177.

B. D. Schmid, W. Weng, **S. Li**, O. Karlström, M. Hupa, Z. Li, P. Glarborg, P. Marshall, M. Aldén. *Gas phase Sulfation of Sodium Chloride and Hydroxide – experiments and modelling*, **Submitted to Fuels**.

1 Introduction

In the global energy system, fossil fuels have been predominated as the primary energy source for centuries, and about 90% of global energy comes from combustion [1, 2]. Overuse of fossil fuels has consequences such as severe air pollution and global climate changes. To overcome this, the demands for renewable energy and alternative fuels are increasing [3, 4]. In this thesis, two solid fuels, biomass and metal fuels, are studied for their combustion behaviors.

The work described in this thesis presents the complex process of biomass char and iron powder combustion. Many biomass fuels contain high amounts of potassium, which can be released in different thermal conversion processes. The potassium release increases the risk of slagging and corrosion in combustion equipment. In this thesis, we focused on the quantitative measurement of potassium released from burning pulverized biomass char particles. This is motivated by the fact that over 80% of the potassium present in the raw biomass can remain in char, despite the char contain no more than ~25% of the initial mass. The fundamental knowledge developed in this thesis can help increase the efficiency of biomass fuel utilization and lower emission.

Metal combustion is a very complicated two-phase flow with both homogenous and heterogeneous chemical reactions. The metallic fuels can be directly burned and release high-grade thermal energy, which can be used directly for industrial applications and residential heating, while the metal oxide product can be recycled and reduced using clean energy such as hydro, solar and wind power [5, 6]. Fig. 1.1 illustrates the concept of a novel zero-carbon energy system using metallic fuels as recyclable energy carriers [3]. In principle, this kind of energy system will achieve zero-carbon and near-zero-pollutant emissions, and stabilize the whole energy system taking into account the unstable production of primary clean energies. Nowadays, iron and aluminum are two potential metal fuel options because of their high energy density, abundant reserves in the earth crust, and well-established powder metallurgy technologies [7, 8].
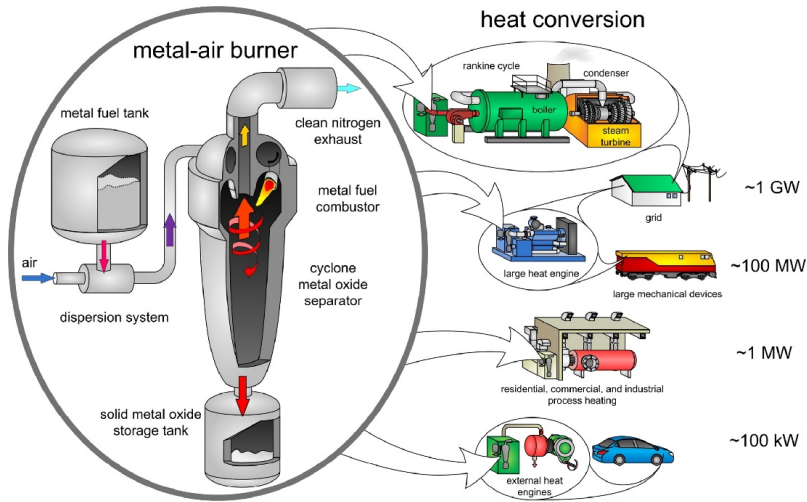
Figure 1.1 Concept drawing of a zero-carbon energy system using metallic fuels as recyclable energy carriers. Reprinted from [3] with permission of Elsevier.

Motivated by the potential need, extensive investigation of iron particle combustion and related pollutant emissions are required. The process of iron combustion needs to be investigated both for single/lower concentration particles and at high concentration of dust cloud combustion conditions. The metal combustion characteristics are mainly determined by the thermo-properties of the metal particle and its oxides [9]. Due to the limited theoretical and experimental work on metal powder suspension combustion, this thesis focuses on fundamental research utilizing in-situ non-intrusive advanced optical diagnostic techniques to investigate the combustion characteristics of metallic (Fe) powder suspensions. A deeper understanding of the combustion process can be achieved with the experimental data fitting to kinetic modelling and CFD simulation. Thus, a more efficient combustor can be developed.

The thesis is divided into two parts based on the fuel types: biomass and metal (Fe) particles. Laser-based diagnostic techniques provide in-situ non-intrusive information of the combustion process with high temporal and spatial resolution [10]. The release of potassium from single burning pulverized wheat straw char particles was quantitatively measured using laser-induced photofragmentation fluorescence (LIPF), which demonstrated that the LIPF imaging method can be used to investigate the potassium release from burning biomass. In addition, this thesis also investigated the combustion characteristics of single pulverized biomass-derived char particles. The char ignition process, total potassium release, and particle temperature has been quantitatively studied. For iron particle combustion, the experiment data of single iron particle combustion is consequently limited. To investigate the metal particles combustion, a new combustion system including a

2

high voltage particle feeding apparatus, a Bunsen burner, and a Mckenna burner has been built and tested to provide reaction environments. The optical method, digital inline holography (DIH), has been developed and applied for detecting burning metal particles. High-speed imaging allows freezing the moving metal particles so that the detailed combustion characteristic can be observed. During the iron particles burning, important phenomena of micro-explosions and nanoparticle release have been observed and investigated using high-speed stereoscopic imaging and shadowgraphy.

1.1 Outline of this thesis

This thesis consists of 6 chapters introducing the subject of advanced optical diagnostics applied in solid fuel combustion. Chapter 1 intends to introduce this thesis with subjects and experiments discussed and presented in the following contents. Chapter 2 covers the basic principle and overview of the experiment devices and techniques applied in this thesis. Chapter 3 describes the detail of the solid fuel and the burners. Chapter 4 presents the combustion characteristics of burning single biomass pellet and biomass char particles. Chapter 5 covers single iron particle combustion. Finally, a summary and future work outlook are discussed in Chapter 6.

2 Experimental equipment and optical diagnostics

2.1 Optical equipment

2.1.1 Lasers

2. 1. 1. 1 Nd:YAG laser

Nd:YAG laser is a solid state laser using neodymium-doped yttrium aluminum garnet crystal (Nd:Y3Al5O12) as the laser medium. It is known as a four-level laser system, where four energy levels are involved when operating the laser system. The Nd:YAG laser system can be operated both in pulsed mode and continuous mode. The fundamental laser beam generated by a Nd: YAG laser is in the near-infrared spectral region at 1064 nm. The higher harmonics laser output 532 nm, 355 nm, 266 nm and 213 nm can be achieved with second, third, fourth, and fifth harmonic generation crystals, respectively. This laser can be used in many diagnostic applications, such as laser-induced incandescence (LII), particle imaging velocimetry (PIV), Raman and Rayleigh scattering measurement.

Most importantly, the Nd:YAG laser can be used for some important fuels and species excitation by generating laser-induced fluorescence (LIF).The laser radiation with wavelengths at 532 nm and 355 nm is commonly used as pump light sources for a dye laser or an optical parametric oscillator (OPO) to generate a tunable laser beam covering a broader wavelength range. The Nd:YAG laser employed in this thesis had a pulse during ~ 10 ns with a repetition rate of 10 Hz.

2.1.1.2   ArF excimer laser

The name Excimer comes from the excited state dimer of the medium from which lasing is generated. Excimer lasers offer an efficient access to ultraviolet (UV) laser beam. The commonly used laser medium is a compound of noble gases, halogen, etc. In this thesis, the multicomponent ArF Excimer laser (Compex 102, Lambda Physik) was used for LIPF measurement of KOH in biomass char combustion. For providing the 193 nm laser beam, the following gas are mixed as the laser medium:

Ar 160 mbar, Ne 2340 mbar, He 400 mbar, and F_2 (5%) in He (95%). The laser pulse duration is around 25 ns and the output pulse energy of 50 mJ.

2.1.1.3   DPSS laser

In the DIH measurement system, a diode-pumped solid-state (DPSS) laser (laserglow Tech., LRS-0457) was employed, where the average output power is 346 mW. It is a continuous-wavelength (CW) laser beam at 457 nm using the second harmonic of a diode pumped $Nd:YVO_4$ crystal. The beam diameter is 3 mm with a near TEM_{00} mode. The laser beam is spatially filtered and collimated into a plane wave of about 40 mm diameter before illuminating the domain of interest in the iron dust flame.

2.1.2   Detectors

2.1.2.1   ICCD cameras

An intensified charged-coupled device (ICCD) camera is an electronic camera with an intensified CCD as the imaging sensor. The intensifier is the most important component of an ICCD camera, which usually consists of the following parts. Photocathode, which converts the incoming photons to photoelectrons. A micro channel plate (MCP) is installed after the photocathode and enormously multiplies the photoelectrons. Then a phosphor screen translates back the photoelectrons to photon, after which the signals are read out on the coupled CCD image sensor. The MCP can act as high-speed shutter when operated in the mode of "gating", which can be gated down to the picoseconds scale. This concise gating time allows the detection of high-resolution laser-induced signals and the possibility of detecting the strong metal particle emission by suppressing the background from flame chemiluminescence. To choose a proper ICCD camera, the quantum efficiency (QE) as a function of wavelength needs to be known. The PI-MAX4 (1024f, Princeton Instruments) ICCD camera with an optimized QE curve in the visible region was employed as a detector for the spectroscopy and metal particle luminous intensity measurement.

2.1.2.2   High-speed cameras

Most high-speed cameras use the complementary metal-oxides-semiconductor (CMOS) sensors due to their possibility of fast reading out compared to the CCD sensors. In a CMOS-based high-speed camera, the light is converted into electrons in form of accumulated charge directly at each pixel sensor first. Then several transistors at each pixel amplify and move the accumulated charge more directly and parallel to read out and digitize the information individually. A trade-off between the temporal and spatial resolution needs to be tested and fixed for high-speed imaging. A high frame reputation rate is accompanied by a smaller imaging

area in which the sensors are used, giving a poor spatial resolution. In this thesis, we had chosen a small region of interest (ROI) that fit the need both for temporal and spatial resolution required. A high-speed camera (Photron FASTCAM SA5, 1024×1024 pixels array, pixel size of 15.7×15.7 μm^2) with 7500 frames per second (fps) was employed to record the moving burning iron particles allowing for the measurements of the whole burning process of iron particles. Two identical high-speed cameras (Phantom VEO 710L CMOS) were placed in a stereoscopic configuration allowing 3D position and 3D velocity measurements and investigating microexplosion of iron particles. The high-speed camera had a resolution of 1280 × 800 pixels with an individual pixel size of 20 μm and 12-bit depth. The resolution was reduced to 1280 × 600 pixels allowing for a frame rate of 10 kHz.

2.1.2.3   *Spectrometers*

A fiber optical spectrometer (USB2000+, Ocean Optics) was employed to capture the UV-absorption spectroscopy, consisting of an analog-to-digital converter, programmable electronics, and a CCD-array detector with 2048-element. This spectrometer can provide spectroscopy with a resolution of 0.1 nm (FWHM) from 200 nm to 850 nm. The wavelength reading of the spectrometer will drift slightly when applied in different conditions and times, which must be calibrated periodically. A light source (Hg-Ar lamp) with more than six spectral lines located in the wavelength region of the spectrometer are used for calibration. A grating-spectrometer (Shamrock SR-750, Andor) is applied to record the emission spectra of iron flame, which is based on Czerny-Turner optical design.

2.1.2.4   *Photodiode*

A photodiode is a semiconductor device with a P-N junction that can convert photons (or light) into electrical current signals. A photodiode (PDA100A2, Thorlabs) is adopted in the moving particles tracking and optical detection system. In the system, a CW laser beam passed through the hot gas flow close to the exit of the central tube of the burner, and the scattering from a particle was detected by photodiode when biomass and char particles passed through the laser beam.

2.2 Advanced optical techniques

2.2.1   Planar Laser-Induced Fluorescence (PLIF)

Laser-induced fluorescence (LIF) is an optical measurement technique widely applied in combustion diagnostics, based on fluorescence emission from the species excited by laser light. LIF is a two steps process: excitation and de-excitation. Firstly, a specific wavelength laser needs to be chosen to match the well-established optical

absorption transition of the monitored species to excite species from the ground energy level to its excited level. Then, a following de-excite process happens with fluorescence emitted due to the energy release from the unstable excited state to its ground state. More details about the LIF principle can be found in the reference [11]. To perform two-dimensional (2D) measurement, planar laser-induced fluorescence (PLIF) was introduced. The laser sheet is passed through and illuminated the field of interest (gas flow). An ICCD camera was installed perpendicular to the laser sheet plane to capture the subsequent fluorescence relaxation event. PLIF is used for detecting concentrations of flame radicals and a range of temperature, velocity, and pressure in different environments. In this thesis, polycyclic aromatic hydrocarbon (PAH) emission during the whole burning history of individual biomass pellets in various combustion atmospheres has been investigated with PLIF measurements.

2.2.2   Laser-Induced Photofragmentation Fluorescence (LIPF)

Many combustion radicals, such as OH, CH, and NO with bonding excited states can be detected using laser-induced fluorescence (LIF). For these species, the LIF signal can be spontaneously emitted after absorption of the resonant photon. However, the concept of laser induced photofragmentation fluorescence (LIPF) can be applied for molecules in the absence of bonding excited states. In LIPF, a pump photon photodissociate a parent molecule into fragments, which can be detected by a probe photon using LIF. Either one or two laser wavelengths maybe used in the LIPF measurement. In one laser wavelength LIPF, the laser should both photodissociate the molecule and electronically excite one of the formed fragments. For the two laser LIPF concept, the pump and probe processes are separated, where all fragments are created in the ground state.

In detecting potassium released, only one laser (ArF excimer) is used for LIPF since it can both photodissociate the potassium hydroxide (KOH) and potassium chloride (KCl) molecules and electronically excite the formed fragments K. The ArF excimer laser sheet at 193 nm was focused into the probe volume to dissociate KOH and KCl to K around the burning char particles, and the signal of the produced fluorescence from the excited K fragments was captured by an ICCD camera located perpendicular to the laser sheet near the probe volume. A band-pass filter at 766 nm was installed in front of the camera to filter the fluorescent emission from exited K. The fluorescence signal is proportional to the concentration of the parent molecule (KOH or KCl).

8

2.2.3 Laser-Induced Breakdown Thermometry (LIBT)

In Fig. 2.1, a plasma source geometry is presented. The breakdown initiates at the lens focal point and then rapid expansion after cooling and collapsing results in a bipolar acoustic pulse. Acoustic-based laser-induced breakdown thermometry (LIBT) was developed as a novel method for gas temperature measurement in combustion atmospheres by analyzing the sound emission from laser-induced breakdown. The detailed measurement procedure has been described in Paper I. In LIBT, the temperature is derived from the accurate measurement of the speed of sound in the environment with known gas composition. The speed of sound in an ideal gas can be written as:

$$V_0 = \left(\frac{kR_0T}{M}\right)^{\frac{1}{2}} \tag{2.1}$$

where k is the specific heat ratio, R_0 is the ideal gas constant, M is the molecular weight, and T is the temperature [12].
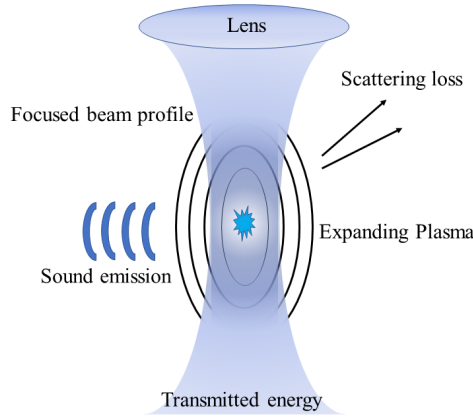

Figure 2.1: Laser-induced breakdown source geometry.

In paper I, two laser-induced breakdown spots are generated and the local gas temperature between these two spots is determined through the sound speed measurement between them. The schematic of the setup is shown in Figure 2.2. A previous study of two plasma points generated simultaneously from the same laser can introduce notable system uncertainty, about 5% to the measured temperature [12, 13]. In the present work, a new measurement procedure was adopted to eliminate the interference, where two individual laser pulses with optimized firing order and delay time were employed. With the new procedure, the system uncertainty caused by local gas breakdown can be largely avoided. The temporal and spatial resolutions can reach up to 0.5 ms and 10 mm, respectively. In previous work [12, 13], the nonlinear region generated by the plasma would influence the

measurement accuracy of sound speed when only one laser is applied because the plasma-generated acoustic wave will inevitably pass through the shock wave region. However, this error can be minimized by using two laser-induced breakdowns in the set-up system due to the same wave propagate mechanism. The error can be canceled by subtraction their time of arrival to the detector.
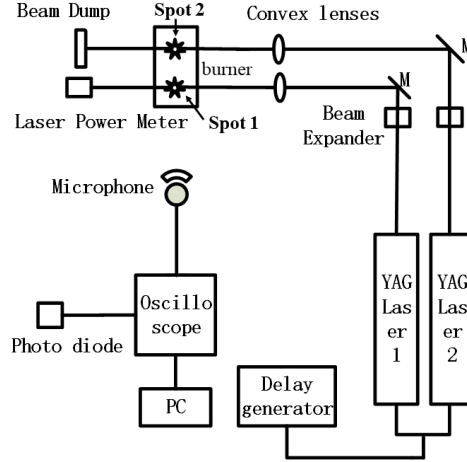

Figure 2.2: Experimental setup for dual-laser-induced breakdown acoustic wave measurement.

2.2.4   Digital Holography (DH)

Digital holography (DH) is a laser-based volumetric imaging technique that can be used to record and retrieve the complex amplitude and phase of a three-dimensional optical field [14-16]. DH can quantify the 3D location and in-plane size and shape of particles using a single camera. Furthermore, combined with particle tracking velocimetry (PTV), 3D velocities can be obtained by tracking particles detected in sequential holograms [17-19]. DH can be divided into off-axis and in-line, based on the angle between the reference wave and object wave. Digital in-line holography (DIH) was adopted in this thesis to generate experimental holograms of particle fields due to its ease of implementation. These holograms were then processed using a clustering-based particle detection (CBPD) method as described in Paper V and other alternative particle detection methods.
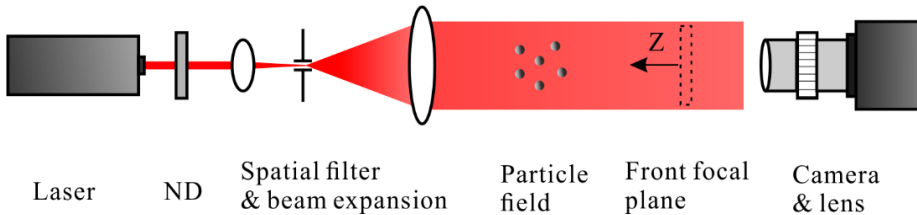
Figure 2.3: A typical experimental configuration of digital in-line holography for particle field measurement. (ND: neutral density filter)

Fig. 2.3 shows a typical experimental configuration of DIH for particle field measurement. The particle field is illuminated by a collimated laser beam, modulated using a neutral density filter and a spatial filter. Then, the forward-scattered light of the particles (i.e., the object wave) interferes with the undisturbed part of the illuminating beam (i.e., the reference wave), which is recorded by the camera to form a digital hologram of particles. In order to alter the magnification, a lens is usually equipped with a camera to capture the hologram [20-22]. More details of the principle of DH can be found in the references [15, 16].

3 Fuels and burners design

3.1 Solid fuels

Solid powders, unlike gases, present very different characteristics depending on the producer and way to fabricate. Powders can burn very differently with the same content and mean diameter because of varying particle morphology and size distribution [23, 24].

3.1.1 Biomass and biomass char

Two biomass fuels, wood, and straw, were prepared in cylindrical pellets with weights of ~300 mg. The wood and straw pellets were around 6 mm × 10 mm and 8 mm × 5 mm (diameter × length). The properties of the biomass fuels are presented in Table S1 in the supplemental material of Paper II. To verify that the LIPF imaging method can be used to investigate the potassium released from burning biomass fuel, the wheat straw char particle was prepared in a drop tube furnace at 1000 ℃ for 2 s in paper III. To extend the study of combustion characteristics of different single pulverized biomass char particles, four types of biomass char particles were prepared from pulverized raw wheat straw (WS), grape pomace (GP), kiwi branches (KB) and rice husk (RH) at a drop tube furnace at two pyrolysis temperate, 1273 K and 1473 K, respectively. All eight char particles are in size range 224 -250 μm. The detailed biomass char properties can be found in Paper IV.

3.1.2 Metal particles

The iron powder used in this thesis is produced by Höganäs AB (NC100.24), which are sponge iron particles with a porous internal structure, and it is one of the most widely used grades in manufacturing sintered parts. It has an irregular surface shape and the spongy structure of its particles, and it has good compressibility due to its low contents of oxygen and carbon (<0.01). The iron particles being studied are sieved through a series of standard sieves connected with a vibrating sifter, which allows selecting the iron powder into several narrow particle size distribution ranges (~20 μm, ~40 μm, ~60 μm, ~80 μm, and ~100 μm). Fig. 3.1 (a) presents the scanning electron microscopy (SEM) image of the sieved sponge iron particle, showing the rough surfaces and porous structures. Fig. 3.1 (b) showed the size

distribution obtained by counting and measuring the particles in the SEM image in Fig. 3.1 (a).
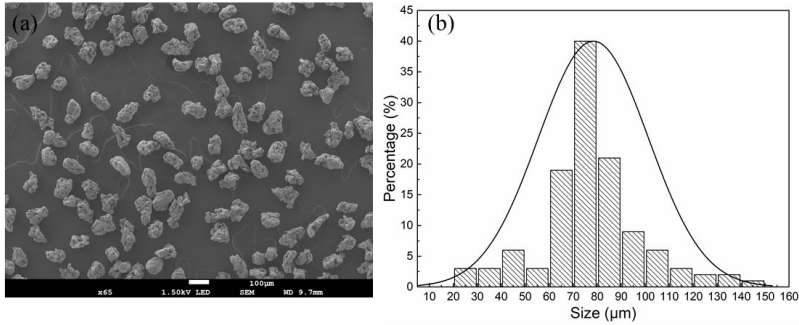
Figure 3.1: SEM image of iron powder of 80 µm samples (a) and the particle size distribution (b).

3.2 Burner design

3.2.1 Multi-jet burner

In this thesis, a newly designed multi-jet burner was adopted to provide uniform hot gas environments, where the absorption spectroscopic techniques can be easily applied due to the uniformity [25]. The gas burner can provide an even and adjustable gas environment with an extensive range of temperature and gas products composition for quantitative experimental measurements. Using the multi-jet burner, the concentration measurements of K atoms are investigated by tunable diode laser absorption spectroscopy. The concentrations of KOH and KCl were measured by broadband UV absorption spectroscopy technique.

Figure 3.2: The structure of the burner (a) A cross-sectional view of the 3D structure of the multi-jet burner. (b) Image of the premixes flame. (c) Photo of the burner. [25]
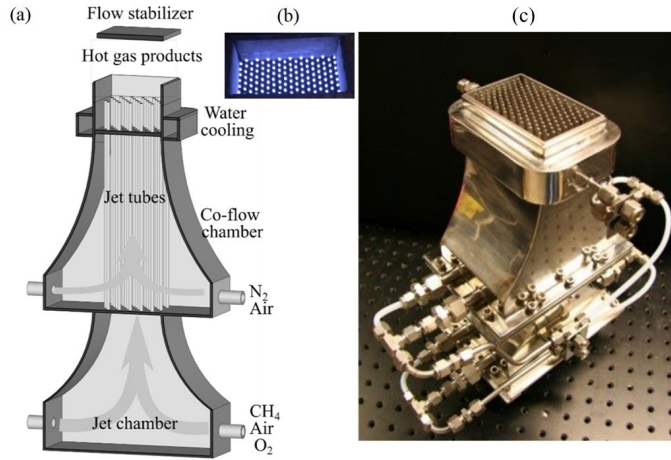
A schematic of the burner is shown in Fig. 3.2 (a) with 3D cross-sectional structure and (c) a photo. The burner has a rectangular outlet with dimensions ~ 85 mm × 47 mm, convenient for applying absorption spectroscopy. The burner consists of jet-flow chamber and co-flow chamber, separated by a divider. The jet-flow can be evenly injected into 181 jet tubes with mainly CH_4/air/O_2 mixture. A laminar premixed small jet flame is stabilized at the top of the jet tube, presented in Fig. 3.2 (b). A co-flow is spontaneously injected into the co-flow chamber to obtain a uniform laminar flow. The flame conditions can be adjusted by varying the gas mixture of the jet-flow and the co-flow, in which both the temperature and the hot gas products composition have an extensive range of variance.

The detailed structure of the multi-jet burner has been presented in Weng. et al's work [25]. The temperature at 5 mm above the burner was measured by Borggren et al. using two-line atomic florescence pyrometry [26] and dual-laser-induced breakdown thermometry as described in Paper I. The equivalence ratio in this work, was changed from 0.6 to 1.3 to provide hot gas products with different O_2% to have temperatures between 1120 K to 1950 K.

3.2.2 Metal-fuel burner

For lab-scale research, it is necessary to provide a long period of continuous laminar flow of metal particles with stable and controllable parameters. This work presents a novel designed versatile particle seeding system. The designed device is similar to the setup developed by Kim [27] and Shoshin [28] [29] [30], based on the electrostatic force particulate method. A similar design has also been applied to investigate the burning time of micron-sized metal particles [31]. Our improved

design could help fulfill some new application features, e.g., controlling particle seeding concertation, jet velocity and providing an extensive range of particle sizes for conductive particles, e.g., metal, biomass char.

A two-dimensional view of the final apparatus is shown in Fig. 3.3, and the essential parts have been marked. The device is based on a high voltage dispersion system to disperse the powder and produce a stable flow of particles. It contains two electrodes, one connects to a high voltage DC power supply, and the other connects to the ground. When conductive particles contact one of the electrodes, they will be charged and repelled from that electrode. Meanwhile, it is also attracted by the opposite electrode, which makes them move toward and recharge upon the collision. The applied electric field can adjust the particle density by changing the distance between electrodes, and it can also be adjusted by varying the voltage supply. A short piece of transparent plexiglass tube is amounted between two electrodes to monitor the particle dispersion inside the apparatus and possible electric breakdown. The outer diameter of the lower electrode (A) was designed to be 55 mm, which features the cup-holder shape acting as a reservoir with a specific holding capacity and reduces particle agglomerations in the edge. Particles are entrained by a central jet flow and left through a 1 mm hole in the top plate. A small gas (CH_4) flow is fed to the dispersion chamber using a mass flow controller system from the bottom of the chamber. After the gas starts entering the capacitor, a gas flow with the particles exits the hole in the top plate of the capacitor, and then mixed with N_2 and O_2 in the inner Bunsen tube. The shroud gas flow was injected through the outer layer of the Bunsen tube to reduce flow disturbance and particle build-up around the central opening. The diameter of the hole is much smaller than that of the top electrode plate. It allows each particle to multiply collisions with electrodes before it exits from the hole, which helps to dissociate the particle agglomerate.
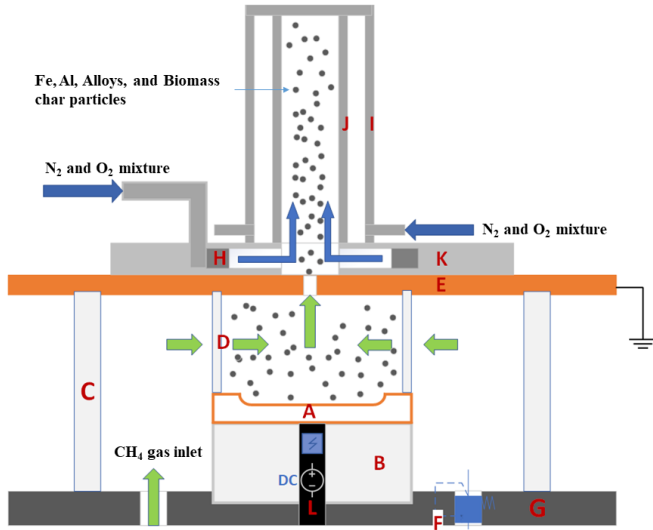
Figure 3.3: Apparatus view with identification of different parts. **A**: Down electrode (HV), **B**: PTFE supporter, **C**: Plexiglas tube, **D**: Porous plastic tube, **E**: Top grounded electrode, **F**: Pressure relief valve, **G**: Base plate, **H**: Flow distributor, **I**: Exterior of the burner, **J**: Inner of the burner, **K**: Top plate, **L**: HV DC cable.
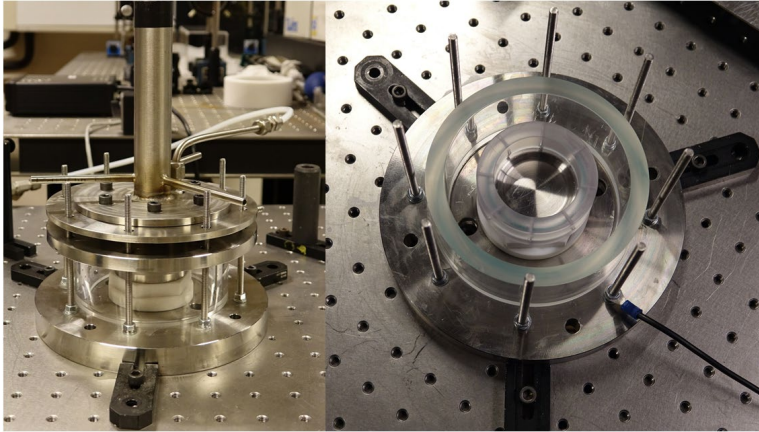
Figure 3.4: Device image and the opening components.

To measure the iron particle seeding density, we collect all particles over a defined time with a collecting plate in the burner exit. The robustness of the powder supply device is of great importance for quantitative studies of iron particle combustion. For all testing cases, the voltage of the capacitor was set to10 kV, and the volume flow rate of the seeding flow (CH$_4$+N$_2$) was set to 3 l/min. Without ignition, the mass flow rate of the ejected iron particles was measured by a real-time weighing system. In this system, a square magnet board (5×5 cm^2) connected to a digital

weighing instrument (A&D FZ-120i, readability: 0.001 g) was placed 1 cm above the burner outlet to collect the ejected iron particles. Due to the strong magnetic force, most of the ejected iron particles were captured successfully. The accumulated weight of the ejected iron particles (80 μm) as a function of time is demonstrated in Fig. 3.5. Quantitatively, based on a high-voltage capacitor, our metal powder supply system can provide a stable mass flow rate of iron particles (~0.852 g/min.) for more than 50 seconds. Therefore, all testing cases in this work were conducted under this stable mass flow rate for comparative studies.
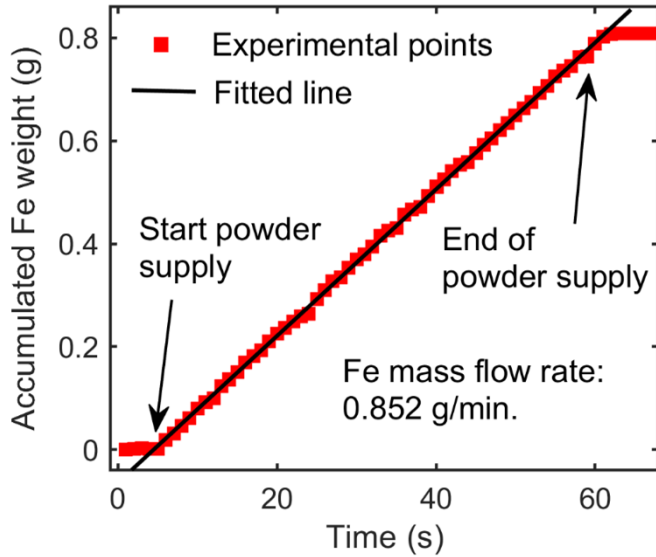

Figure 3.5: Accumulated weight of the ejected iron particles as a function of time. A linear trend demonstrates a constant flow rate of particle injection over 50 seconds.

The set-up for the flame characterization of micro-sized metallic powder and biomass char powder were performed. The dispersion behaviour of different powders could be influenced by particle size, shape, chemical and moisture content.
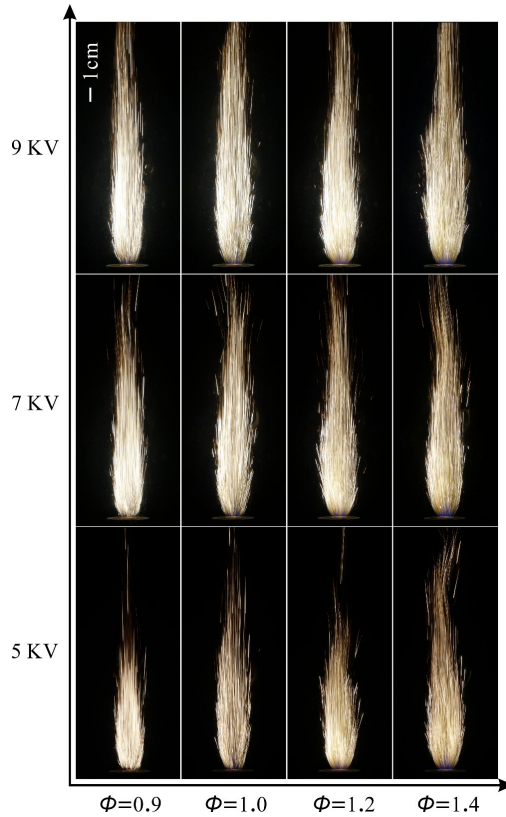
Figure 3.6 Flame of the iron particles (40 μm) combustion in a Bunsen flame.

Fig. 3.6 shows burning iron particles (40 μm) in a $CH_4/N_2/O_2$ premixed Bunsen flame acquired by a high-resolution digital camera. The operating conditions are summarized in Paper VII. The brightness of the flame increase and the burning time decrease when the oxygen concentration increases (case 4 to case 1). The flame structure becomes higher when the power supply increases. The seeding concentration changes from 20 g/m^3 to 290 g/m^3 when the voltage supply increases from 5 kV to 9 kV, making the oxygen consumed faster and driving the iron particles to burn longer.
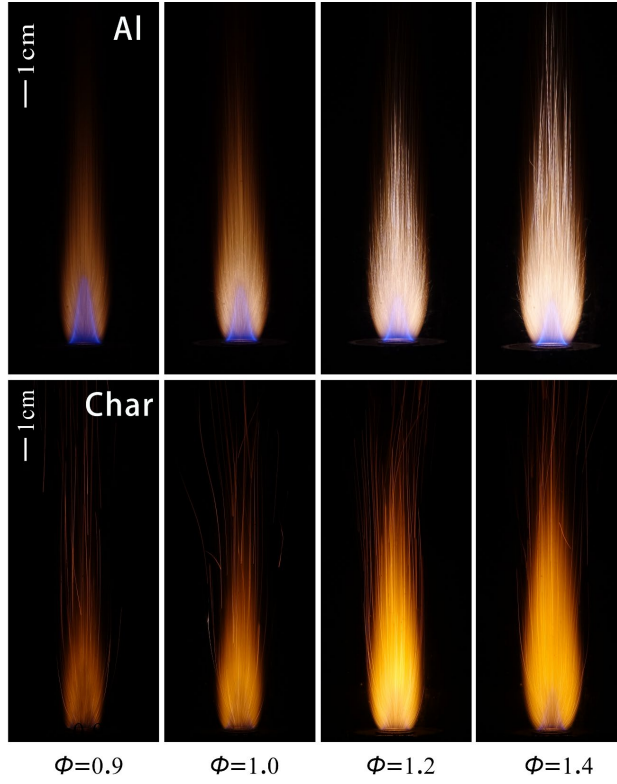
Figure 3.7: Flame of the aluminum particles (37 μm) and char particles (224-250 μm) combustion in a Bunsen flame.

The aluminum and biomass char particles combustion at flame condition case 3 are shown in Fig.3.7. A laminar aluminum aerosol flame is obtained at the exit of the nozzle. The flame structure changed with the oxidation environment from lean to rich. The height of the aluminum flame increase when the oxygen concentration decrease. The large micron-sized aluminum particles can combust and stabilize in a $CH_4/N_2/O_2$ premixed Bunsen flame. This work also presents the first attempt to seed biomass char particles with different densities by applying an external electric field in a well-controlled laminar premixed flame.

4 In situ quantitative measurements from burning biomass pellet and biomass char particles

4.1 Single biomass pellet combustion

In the present work, accurate in-situ optical measurements over burning biomass pellets, including surface temperature, volatile gas temperature, polycyclic aromatic hydrocarbon (PAH) emission, and mass loss over individual biomass pellets during the whole burning history, have been made. A detailed experimental setup is shown in Fig. 4.1, with measurement techniques and the flame conditions introduced in Paper II. The gas temperatures were measured using TLAF thermometry with indium atoms [26].

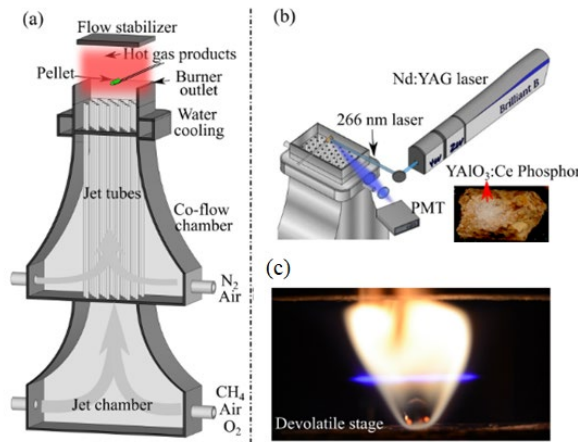**Figure 4.1:** Schematics of the multi-jet burner (a), the experimental setup of phosphor thermometry (b), and the LIF images of atomic indium above the burning wood pellet at de-volatilization stage (c).

The flame conditions adopted in the present study are presented in Table 4.1. The temperature in the table was measured using TLAF thermometry by seeding indium atoms, as described by Borggren et al. [26].

Table 4.1 Operating conditions.
Summary of the flame conditions adopted in this experiment. The temperature was measured at 5 mm above the burner outlet.

Flame Case	Gas flow rate (sl/min)					Fuel-air equivalence ratio φ	Gas product temperature (K)	O$_2$ in gas products (%)
	Jet-flow			Co-flow				
	CH$_4$	Air	O$_2$	N$_2$	Air			
T1O1	2.66	17.34	1.89	10.83	7.74	0.74	1750	4.5
T1O2	2.66	17.34	1.89	18.60	0.00	0.96	1790	0.5
T1O3	3.04	17.11	1.86	13.95	0.00	1.12	1840	0
T2O1	2.47	12.23	2.58	18.97	8.90	0.70	1550	4.5
T2O2	2.47	12.23	2.58	27.90	0.00	0.96	1530	0.5
T3O1	2.28	11.89	2.26	22.69	9.83	0.67	1390	4.5
T3O2	2.28	11.89	2.26	32.55	0.00	0.96	1400	0.5

4.1.1 Surface temperature

The surface temperature of burning biomass pellets was accurately measured using phosphor thermometry. Two phosphors, Mg$_4$FGeO$_6$:Mn and YAG:Tb, were used to measure the surface temperatures of burning pellets at low and high temperatures with the lifetime method. The correlation between temperature and the decay time was obtained using the calibration procedure reported by Nada et al. [32].

The phosphor powder was placed on the pellet surface as approximately 4 mm diameter spots. Keeping the phosphor coating thin is desirable to minimize potential temperature gradients across the sensor material. The mean thickness of the layer was estimated to be around 2 μm and should, therefore, give negligible temperature gradients. The influence of the phosphor on the char oxidation was also observed to be negligible, as at this stage, only dispersed phosphor particles remained on the pellet surface.
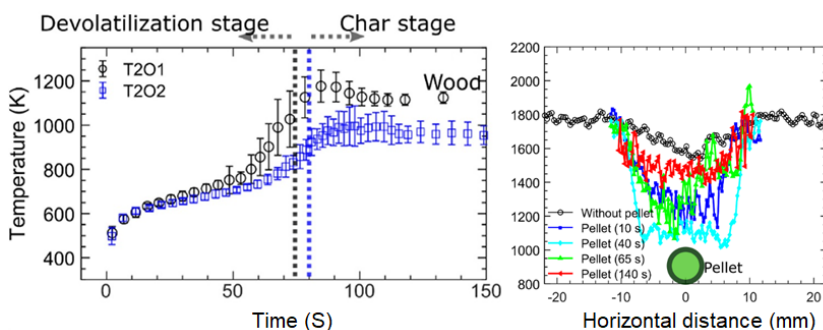

Figure 4.2: Surface temperatures of individually biomass pellets of different flame conditions over the burning time (left) and Temperature distribution of the gas 5 mm above an individually burning wood pellet in the hot flue gas T1O2 (right).

In Fig. 4.2, the surface temperature was lower than the surrounding gas temperature, which indicates that the burning char had significant heat losses through thermal radiation and heat conduction through the holders. Based on mass and mass-loss rates of individually burning biomass pellets in different hot gas flows as a function of the residence time, the devolatilization stage (the mainly mass-loss occurred) and char stage will be separated. The detailed discussion can be found in Paver II. A relatively low surface temperature during the devolatilization stage, ~700 K, was observed on the burning pellets. The volatile gas temperature was ~1100 K and ~1500 K 5 mm above the top of the pellets in a gas environment at ~1800 K with 0.5% and 4.5% oxygen, respectively. During the char conversion, the surface temperature significantly increased during char burning but was still ~500 K lower than the hot gas environment.

4.1.2 Polycyclic aromatic hydrocarbon (PAH) emission

In order to correlate the volatile gas release with the measured surface and volatile gas temperature, the distribution of PAH in the volatile gas above the burning biomass pellets and the release history in different hot gas environments was obtained and is shown in Fig. 4.3. PLIF measurement was adopted to monitor the PAH distribution released from the burning biomass pellet during the de-volatilization stage. The fourth and third harmonic of the Nd:YAG laser (Brilliant B) provided the 266 nm and 355 nm laser pulse, respectively, which were used as the excitation source separately. The laser beam was formed into a sheet of ~1 mm thickness above the burning biomass pellet in the vertical plane. The fluorescence at 410 nm and 515 nm was captured by an ICCD camera (Andor iStar, 1024 × 1024 pixels) simultaneously through a stereoscope lens having 410 nm and 515 nm band-pass filters (FWHM = 10 nm) in each channel.
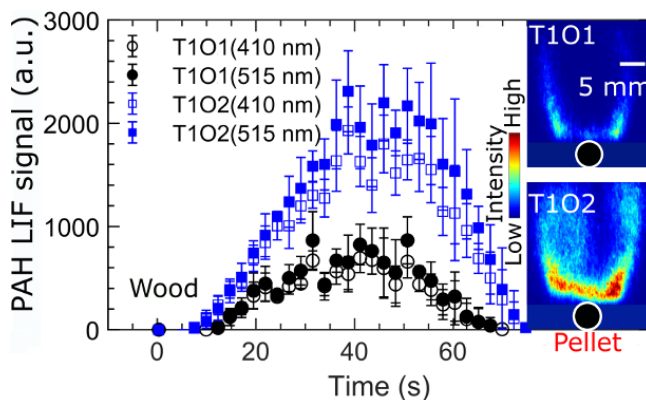

Figure 4.3: LIF signal of the PAH in the volatile above the single burning biomass pellet. Insets: Images of the 410 nm LIF signal at a residence time of 40 s.

The distribution of PAH in the volatile gas above the burning biomass pellet and the PAH release history in different hot gas environments are presented in Fig. 4.3. The fluorescence signal at 410 nm and 515 nm are from the relative light and heavy PAH molecules, respectively [33]. The PAH mainly existed in the region close to the surface of the pellets and was consumed quickly downstream. During the de-volatilization stage, in the first 10 s, the surface temperature increased quickly to ~600 K through a drying process. Then, the PAH started to be generated, and the surface temperature was kept at around ~700 K until the end of the de-volatilization stage. The released PAH shifted towards lighter molecules as the surface and volatile gas temperature decreased with the gas environment temperature.

4.2 Biomass char combustion

Many biomass fuels contain high amounts of potassium, which can be released in different thermal conversion processes. From the study of biomass char, over 80% of the potassium present in the raw biomass can be retained in the char, despite the char generally does not represent more than ~25% of the initial mass. For example, the char from wood biomass combust in flame case T1O1, the initial mass of the pellet was ~300 mg, and after the devitalization, around ~ 45 mg char was left. Potassium release increases the risk of slagging and corrosion in combustion equipment [34]. Paper III and Paper IV provide quantitative experimental data of potassium released from burning single pulverized micrometer-sized biomass particles. [35, 36]

4.2.1 Potassium release

In paper III, the release of potassium from single burning pulverized wheat straw char particles was quantitatively measured for the first time. LIPF imaging was used to measure the two-dimensional distribution of KOH/KCl to study K release from burning wheat straw char particles. The char particles were injected upward into a hot flue gas flow, with a mean temperature of 1580 K and a mean O_2 concentration of 6.5vol.%.

To establish the correlation between the photofragmentation fluorescence signal and the concentration of KOH/KCl an in-situ calibration process was introduced. The LIPF signal from KOH/KCl was calibrated using the multi-jet burner as described above, which provided homogenous hot gas products containing known amounts of KOH and KCl. To calibrate the LIPF signal, the concentrations of KOH and KCl in the hot gas products were measured using UV-absorption spectroscopy. Details of this technique can be found in Weng et. al. [37]

In the hot gas products environment seeded with KOH and KCl, the concentration of K atoms should be considered even though it is negligible compared to that of KOH and KCl. The K atoms can have strong absorption of the fluorescence produced by the photofragmentation process. The correction of the obtained LIPF signal was needed. Hence, in the present study, the concentration of K atoms was measured together with the concentration of KOH and KCl. A TDLAS system with a 769.9 nm continuous-wave laser was used, as discussed by Weng et al. [38]. The correlations (after corrections) between the fluorescence signal and the concentration of KOH and KCl were fitted as follows,

$$N = 1.437 \cdot 10^{15} \cdot S^2 + 1.420 \cdot 10^{17} \cdot S \qquad (4.1)$$

for KOH, and

$$N = 2.596 \cdot 10^{14} \cdot S^2 + 1.583 \cdot 10^{16} \cdot S \qquad (4.2)$$

for KCl, where N is the number density of KOH or KCl and S is the fluorescence signal. However, the signal after the correction did not increase linearly with the concentration of potassium. Another self-absorption should be considered. The exited K atoms were produced by the photodissociation of KOH and KCl, which quickly de-excited to the ground state through spontaneous transition and collision quenching. In this process, part of the spontaneous fluorescence emission was self-absorbed by the atoms in the ground state. Combing the de-excited process and the absorption process that occurred in the probe volume using the Beer-Lambert law, a self-absorption rate with a value of up to 60% was obtained in the case with 20 ppm potassium seeding. After the correction, a good linear correlation between the fluorescence signal and the concentration of the potassium was built as follows,

$$S = 5.286 \cdot 10^{-18} \cdot N \qquad (4.3)$$

for KOH, and

$$S = 1.416 \cdot 10^{-17} \cdot N \qquad (4.4)$$

for KCl. According to the ratio between the slope of these two equations, it was determined that the fluorescence produced from KOH was about 37% of the one from the same amount of KCl.
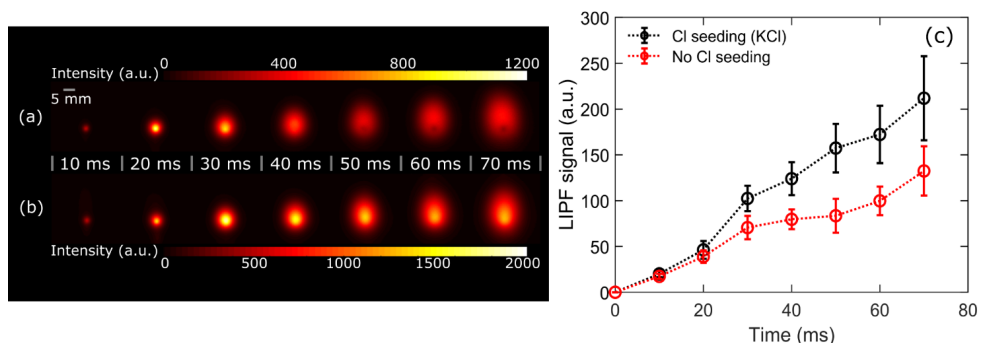
Figure 4.4: Temporal image sequences of the average LIPF signal around a single burning pulverized wheat straw char particle in the hot gas products without Cl seeding (a) and with 320 ppm Cl seeding (b). Average intensities of the LIPF signal versus residence time (c).

Using the correlations between the fluorescence signal and the concentrations of KCl and KOH, expressed by Eqs. (4.3) and (4.4). The average of the signals in Figs. 4.4 (a) and (b) is presented in Fig. 4.4 (c). For both cases, the signals increase almost linearly with the residence time, indicating that potassium is released continuously from burning char particles during oxidation. Comparing the intensity from (a) and (b), the signal from the case with Cl seeding was almost twice as high without Cl seeding. Considering that the fluorescence yield of KOH was about 37% of that of KCl, the results indicate that over 60% of potassium surrounding the burning char particles, initially in the form of KOH, was presumably converted into KCl with Cl seeding.

Using the results of the concentration distribution and considering that most potassium clouds have an axisymmetric structure, as shown in Fig. 4.4 (a), regardless of the shape of char particles, the total amount of potassium released from the char particles as a function of the residence time was obtained through a volume integral. The release rate of potassium remained has been measured during the oxidation period until 70 ms, which was estimated to be 0.5 µg/s. Moreover, the particle temperature was determined using two-color pyrometry that is detailed in Paper III. During the entire burning period, the particle temperature remained at a quasi-constant temperature of ~1600 K, slightly over the surrounding gas temperature.

Single moving biomass particles, without mutual interference, are critical to enhancing the understanding of potassium release behavior in thermochemistry conversion processes of biomass particles and support the development and validation of numerical models [39, 40].

5 Single iron particles combustion

Metal fuels have been presented as a promising option for an alternative and clean energy source. For decades, metal has been investigated as additives in propellants, pyrotechnics, and other energetic materials [41, 42]. The volumetric and gravimetric energy density for various metal fuels compared to batteries, hydrogen, bio-derived fuels, and fossil fuels are shown in Fig 5.1.

For accurate modelling of metal powder combustion and designing reliable high power devices using metal fuel, the most crucial issue is understanding the whole combustion process of metal powder. Metal combustion research can be categorized in different ways. Firstly, the metal particles can be ignited by a laser or other source and combusted one by one [43]. Secondly, metal particles are combusted as propagating dust flames, consisting of single burning metal particles that intensive oxidation/reaction happens during the heterogeneous combustion of metal powders [44, 45]. Thirdly, metal powders can be seeded into another gas fuel to form a hybrid flame, increasing the heat release as heterogeneous combustion [46]. For metal flame, it is hard to generate a stable self-sustain flame. However, it is possible to produce a self-sustaining metal flame with small micron-size particles [47, 48].
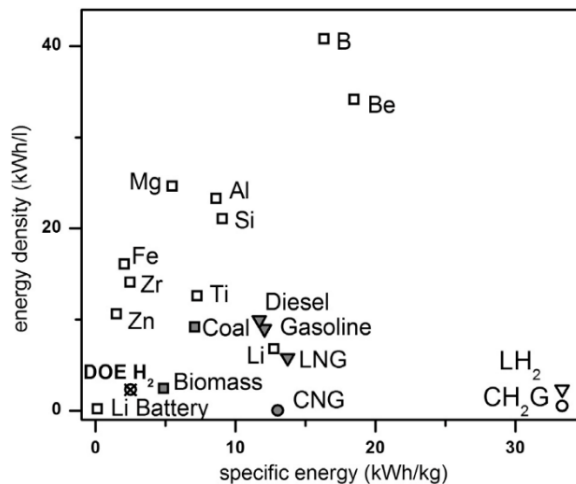

Figure 5.1: Volumetric and gravimetric energy density for various metal fuels compared to batteries, hydrogen, bio-derived fuels, and fossil fuels. Figure reproduced from reference [49] with permission of Elsevier.

The combustion modes of metals are proposed for metal combustion to understand the metal combustion process. As reported by Bergthorson [49-51], a single metal particle can burn in three combustion modes, which are mainly influenced by the metal flame temperature relative to the boiling point of the metal. The three suggested combustion modes are presented in Fig. 5.2.
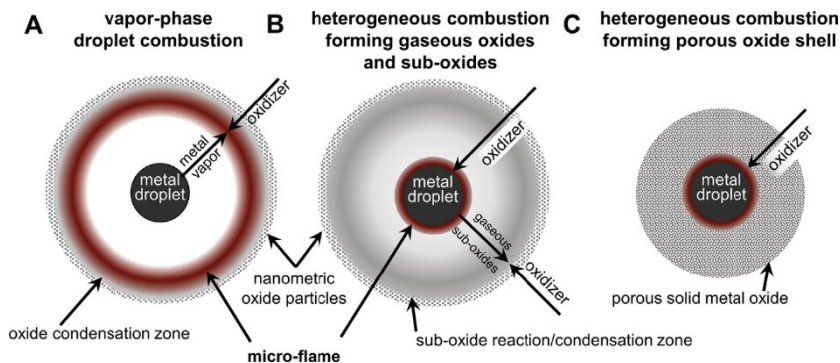

Figure 5.2: Modes of metal particle combustion in the small Biot number regime. Adapted from [49] with permission of Elsevier.

In condition (A), the flame temperature is above its boiling point. The metal droplet can be heated to vaporize as metal gas and then burned in a micro-diffusion flame. In mode (B), the flame temperature is lower than the boiling point of the pure metal, the metal does not evaporate and particles must burn heterogeneously through surface reaction. The nano-sized metal oxides or sub-oxides gaseous were formed around the metal droplet surface, which diffused away from the droplet. Mode C is similar to mode B, except for the condensed oxide formed on the metal surface, leading to a final metal-oxide particle size larger than the initial metal particle.

It is clear that having a metal fuel combusts in mode C is preferable since it is easier to collect the oxides for metal recycling. Bergthorson et al. [49] proposed that iron is a promising metal fuel that can combust in mode C. The formed combustion products can be collected and recycled to form a metal fuel loop. In practice, iron dust combustion will take place instead of single particles. However, the iron dust flame consists of single burning iron particles where intensive oxidation/reaction happens during the heterogeneous combustion of iron powders [52, 53]. The combustion properties of individual burning iron particles thus play an essential role in characterizing iron dust flame where the direct interaction in an iron dust flame between individual particles are rare due to the relatively large distance among particles.

It should be noted that the metal combustion modes are proposed for metal particles burning within the small Biot number regime (Bi ≪ 1) [50, 54]. In this thesis, an extensive iron particle size range has been investigated. Thus, the combustion mode

for larger size iron particles can be different, where a hybrid combustion mode combined mode B and mode C might be expected.

5.1 Characterization of single iron particle combustion

5.1.1 Particle velocity, size, and number density

In the cold flow, the velocities of injecting iron particles are measured using shadowgraph and particle tracking velocimetry (PTV), which are compared with the mean gas flow speed. Iron particles are extracted from each shadowgraph using an optimal threshold, which is then matched with each other using the Simple Tracker [55] to obtain the displacement of each particle. The high-speed imaging of injecting iron particles in the cold flow with N_2 gas as the carrier is shown in Fig. 5.3 (a). The planar velocities of iron particles are derived from the particle displacement and the time interval between two sequential frames. The results of all cases are shown in Fig. 5.3 (b). As expected, the mean velocity of large particles (i.e., D = 100 μm) is significantly lower than that of small particles (D = 40 μm), while the voltage has a much less effect on the particle velocities.
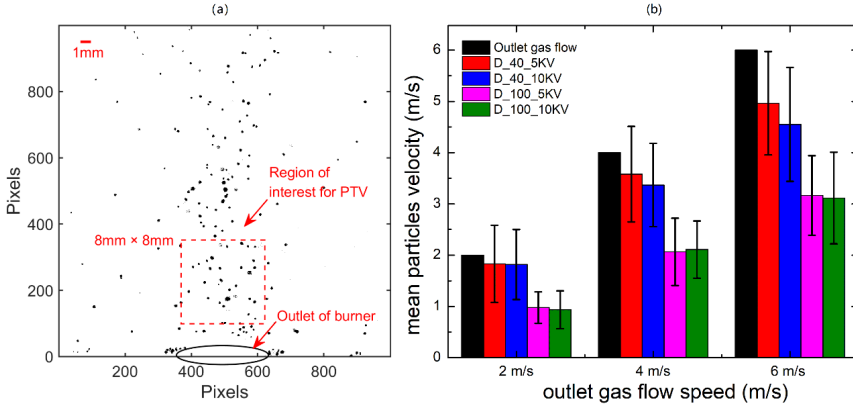
Figure 5.3: High-speed imaging of injecting iron particles in the cold flow with N2 gas as the carrier in a modified Bunsen burner (a) and the derived mean particle velocity in the region of interest by PTV (b).

In the hot gas flow, metal particle combustion is a complex process with intense reactions that result in shape, composition, velocity, and temperature changes. To investigate the 3D metal particle fields, traditional optical diagnostic techniques like direct 2D imaging (e.g. PTV, shadowgraphy [56]), are unable to illustrate the 3D information of the metal particle fields [57]. In addition, direct imaging usually gives a narrow depth of field (DOF) when detecting volumetric metal particle fields with different particle sizes and number of densities. As shown in Fig. 5.4, direct

images of the burning iron particles in a laminar premixed Bunsen flame are taken using a high-speed camera. Most burning particles are out of focus with blurred particle edges because of the narrow DOF, which usually leads to the wrong estimation of particle size and particle number density. Although some burning particles are focused, the information on particle morphology is missing due to the intense light originating from particle combustion. Thus, it is difficult for this direct imaging technique to perform quantitative diagnostics on the iron dust flame. Therefore, digital holographic imaging (DIH) is introduced, capable of re-focusing the objects of interest in a relatively wide DOF.
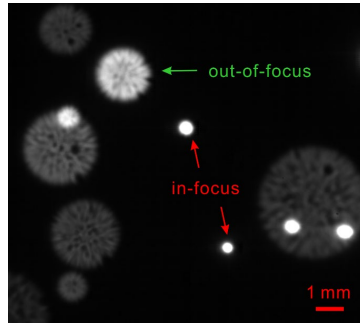
Figure 5.4: A direct image of the burning iron particles (32% O2, y=15 cm) captured by the high-speed camera. The red and green arrows indicate in-focus and out-of-focus particles, respectively.

In Paper VI, iron particles are combusted in a modified Bunsen burner with a stable metal powder supplying system. High-speed digital in-line holography (DIH) is employed for the 3D particle field reconstruction and simultaneously quantifies the 3D particle location, size, velocity, and concentration of burning iron particles. The schematic of the experimental setup is shown in Fig. 5.5.

Figure 5.5: Schematic of the experimental setup. Top (a), the optical arrangement for the high-speed digital in-line holography measurement system. Bottom (b), the iron powder supplying and burning system.

30

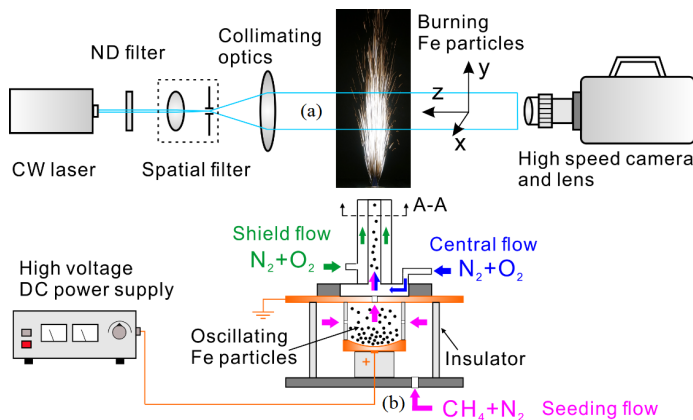The captured holograms were processed by a clustering-based particle detection (CBPD) method, which directly recognized the regions of particles, particle edges and background using multi-dimensional features extracted from the stack of reconstructed images. The schematic of the CBPD method and detailed description can be found in Paper V. There are mainly four steps in processing a holographic image using the CBPD method. Firstly, both the reconstructed images and the corresponding gradient maps are utilized to extract multi-dimensional features in a local region of interest (ROI) where particles may exist. For example, a local ROI is marked in the orange square in Fig. 5.6 (a), which is automatically segmented using the optimal global threshold [58]. Secondly, with the extracted multi-dimensional features, K-means clustering [59] is performed in all pixels of a local ROI to identify three distinct regions (i.e., particle body, particle edge, and background). As shown in Fig. 5.6 (b) and (c), three distinct regions are successfully separated by K-means clustering and obtaining a crude particle edge. Thirdly, density-based spatial clustering of applications with noise (DBSCAN) [60] is performed in the crude particle edge to refine the particle edge and remove noise. Thus, as demonstrated in Fig. 5.6 (d), the refined particle edge is accurately extracted by the DBSCAN clustering. Finally, the refined particle edge is used to determine the depth, in-plane size and shape of the particle in the local ROI. For instance, the binary image and the re-focused image of the particle with an irregular edge are shown in Fig. 5.6 (e) and (f), respectively.
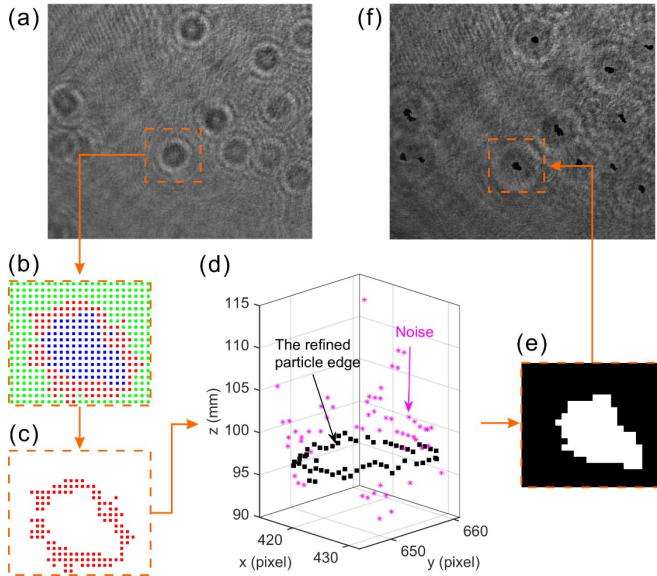
Figure 5.6: A holographic image processed by the clustering-based particle detection (CBPD) method. (a) The raw hologram, (b) The results of K-means clustering (green pixels: background, red pixels: particle edge, blue pixels: particle body), (c) The extracted crude particle edge, (d) The results of DBSCAN clustering (the black squares: the refined particle edge, the purple stars: noise), (e) The binary image of the particle, (f) The re-focused image of the particle.

The 3D reconstruction of the burning iron particle field (40% O$_2$, y = 5 cm) is demonstrated in Fig 5.7. Firstly, the background noise reduction is performed on each hologram before the numerical reconstruction to improve the signal-to-noise ratio of the holograms. Fig. 5.7 (a) shows an example of the denoised hologram. The concentric circular fringes are different from each other, indicating different depths and sizes of the iron particles. Then, most of the burning iron particles can be successfully identified. The corresponding binary image extracted by the CBPD method is shown in Fig. 5.7 (b). In addition, three re-focused burning iron particles with different depth and size are shown in Fig. 5.7 (c). These particles correspond to the diffraction patterns in Fig. 5.7 (a), which are enclosed in the red boxes and labelled as A, B, and C, respectively. Fig. 5.7 (d) visualizes the 3D distribution of the particles in the reconstructed volume. A single example of the iron particle field is given in Fig. 5.7 (d). It is observed that the 3D distribution of the particles is non-uniform within the reconstructed volume. Paper VI shows detailed statistical results about the particle velocity, particle size distribution, and the number density in three iron dust flames with oxygen volume fractions varying from 24% to 40% obtained and compared at different heights above the burner.
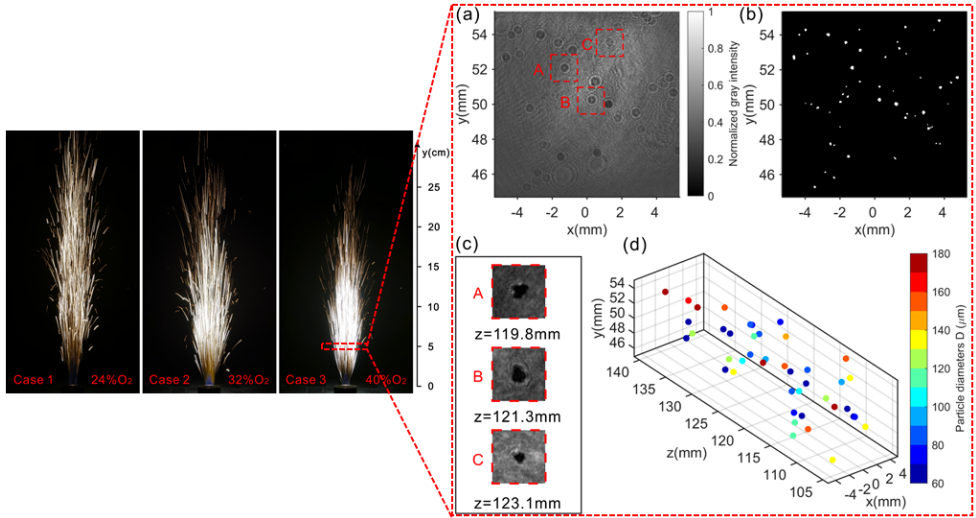
Figure 5.7: Reconstruction in 3D of the burning iron particle field (40% O$_2$, *y* =5 cm). (a) The hologram with background noise reduction; (b) The corresponding binary image extracted by the CBPD method; (c) Three examples of re-focused burning iron particles; (d) The reconstructed 3D distribution of the iron particles with different particle sizes.

Based on the analytical results from Paper VI, some typical features of the iron dust flame were observed along the height direction (y axis). The vertical velocity of the particles gradually decreases with height because of gravity. Furthermore, as oxygen volume fraction increases, the combustion of iron particles becomes more concentrated, making the particles move radially outward faster while reducing the

32

height of the iron dust flame, which is consistent with the iron flame shown in Fig. 5.7. The violent combustion of iron particles accelerates the ejection of the particles radially outward from the central region of the iron dust flame, resulting in non-uniform spatial distribution of the particles and reducing the particle number density in the measurement volume. Besides, the particle size distribution shifts to large particles from the ignition region to the post-combustion region, which validates the swelling phenomenon of iron particle oxidation. Lastly, as the height increases, the particle number density decreases due to the intense thermal expansion of iron particle combustion and then increases due to the slower particle velocity. The results demonstrate that DIH is a powerful tool for in-situ, quantitative characterization of particle dynamics in iron dust flames.

5.1.2 Single iron particle burning
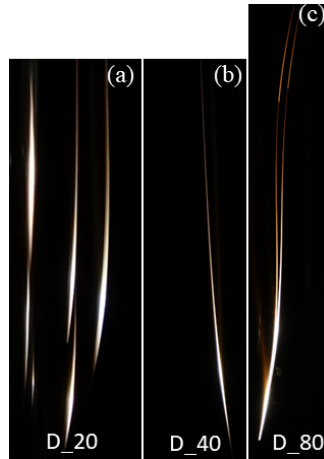
Figure 5.8: Typical images of burning single iron particles with sizes 20 µm (a), 40 µm (b) and 80 µm (c) in premixed McKenna flat flame. The exposure time is 100 ms.

The burning behavior of the single iron particles in a premixed $CH_4/N_2/O_2$ flame showed that these particles gradually burn out as expected. After ignition, the emission intensity of the burning particles increases until it reaches its maximum and then decreases gradually, while a second peak frequently appears before burning out completely. These behaviors are shown in Fig. 5.8, and a detailed explanation of the intensity change are discussed in the following.

5.1.2.1 Fuel and Oxidizer

Table 5.1 Operating conditions.
Summary of the flame conditions adopted in this experiment located at 5 mm above the burner outlet.

Flame	Fuel mixture components (SL/min)			Combustion products composition (vol.%) *				Equivalence ratio φ	Gas product temperature (K)
	CH_4	N_2	O_2	O_2	CO_2	H_2O	N_2		
Case 1	1.60	9.67	12.81	39.9	6.6	13.2	40.1	0.25	1770
Case 2	2.24	9.39	12.45	33.3	9.3	18.7	39.2	0.36	1950
Case 3	2.90	9.11	12.07	26.1	12.0	24.1	37.8	0.48	2200
Case 4	3.74	8.74	11.58	17.0	15.5	31.1	36.4	0.65	2350

* Calculated assuming complete oxidation of CH_4.

All the flame condition used in the single iron particle combustion are presented in Table 5.1. The flame temperature for different flame conditions was calculated by an OPENFOAM solver. The burning times of iron powders in four different oxidizing environments were tested. The high-speed videos capturing these burning particles were processed automatically using a MATLAB script.

5.1.2.2 Experimental Apparatus

In paper VIII, a serious of experiments have been performed to study single iron particle combustion characteristics. The schematic setup is shown in Fig 5.9. The device contains a particle seeding apparatus and a burner device. A Mckenna burner with a central opening was used for the burning part to provide an adjustable premixed flat flame to combust the injected iron particles. To measure the combustion times of the particles, a high-speed camera (Photron FASTCAM SA5, 1024×1024 pixels array, pixel size of $15.7×15.7$ μm^2) with 7500 frames per second (fps) was employed to capture the ignition events visually. The pyrometric particle temperature was measured using an ICCD camera (Princeton Instruments, PI-MAX4 1024f).
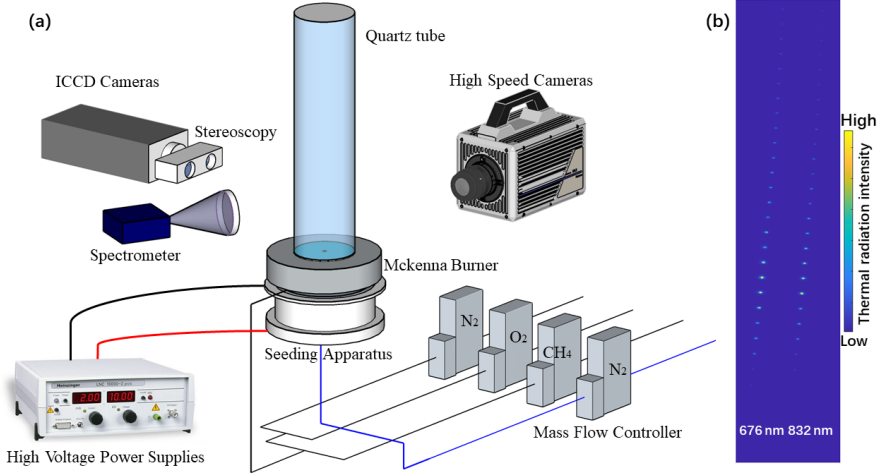
Figure 5.9 Schematic of the experimental setup for the measurement of particle temperature using two-color pyrometry (a), and typical sequences of instantaneous images of the thermal radiation signals at 676 nm and 832 nm during the combustion of single iron particles (b).

5.1.2.3 Combustion time of single particles

To reveal the combustion regime of the burning particles, accurate measurements of burning time and temperature of the single-particle evaluation are essential. Many experimental works have been reported for aluminum [7] and other single metal particles [11,12,49,57]. The Glassman's criterion [61, 62] for vapor phase metal combustion states that for a metal particle to burn in the vapor phase the metal flame temperature should be higher than its boiling point (T_b). In this case, the metal will vaporize and diffusive to the oxidizing environment and react with the oxidizer in the gas phase. Meanwhile, the metal will evaporate due to the thermal heat diffusion. Otherwise, it will happen as a heterogeneous surface reaction/oxidization. The phase of the combust products relies on the metal and the metal oxide properties and the reaction energy released during the metal oxidization.

The combustion time of a single burning particle is an essential parameter in combustion theory and models. It has been shown that metal particles can burn in a kinetic regime, a diffusive limit regime or a mixed regime, directly related to the particle size [12] [52].

In a kinetically controlled combustion, the single iron particle combustion time is proportional to the particle diameter [61-63],

$$t_{b,kin} = \frac{\rho_s d_0}{2 i m_{0,\infty} k_s} \tag{5.1}$$

ρ_s : particle density, d_0 : particle diameter, i : the mass stoichiometric index

$m_{0,\infty}$: oxygen mass fraction, k_s: kinetic rate constant.

In a diffusion-controlled mode, the combustion time linearly increases with the square of the particle diameter when particles are burning [63, 64],

$$t_{b,diff} = \frac{\rho_s {d_0}^2}{8\rho D \ln(1+im_{0,\infty})}$$

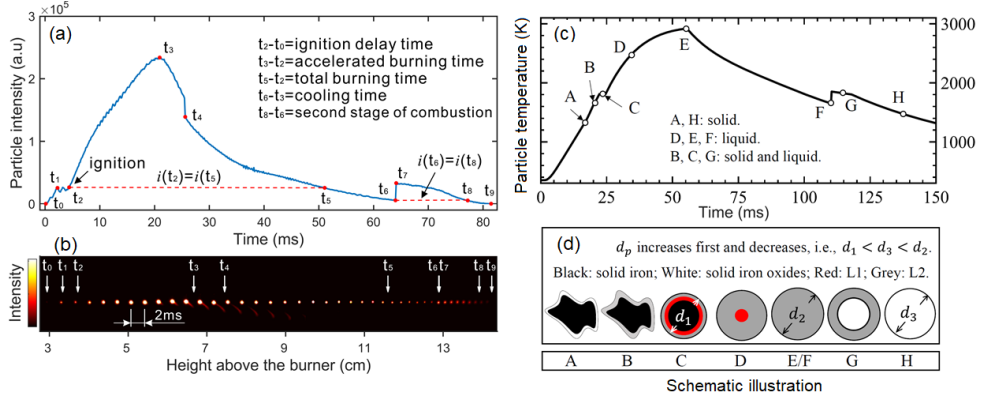(5.2)

ρ: gas density, D: gas diffusivity.

Figure 5.10: (a) Single burning iron particle (80 µm) intensity changes as a function of the particle residence time in flame case 3 with O_2 vol. 26.1%. (b) Temporal evolution of the thermal radiation intensity of the single iron particle captured by the high-speed camera. (c) The corresponding particle temperature (Tp) predicted by simulations and each special characteristic time-point have been marked. (d) Schematic illustration of the five stages in iron combustion.

A typical sequence of instantaneous images of the thermal radiation signals of burning single iron particle is shown in Fig. 5.10 (b). The single iron particle combustion consists of several steps to describe the heat release and phase transition within the residence time. Several representative points have been marked from t_0 to t_9 in Fig 5.10 (a) and (b).

The total burning time is counted from the start to the end of combustion. The signal intensity threshold was set to 20 counts where the background noise was less than 5 counts. The particle surface temperature in the high oxygen concentration can increase to a high level that part of the images may contain saturated pixels. The photon energy of a saturated pixel would dissipate to its neighbour pixels, resulting in a higher integrated intensity or a large particle size of pixels. Such particles are discarded.

Based on our experimental results, the oxygen concentration and particle size influenced the ignition delay time and total combustion time. The effect of particle sizes on the total burning time was much more significant than oxygen concentration when the particle size is larger than 40 µm. The smaller iron particle was easier to

36

be oxidized in the same oxidizing environment. As the iron particle diameter becomes larger, the particle size dramatically influences the oxidizing process during combustion. The combustion time was seen to be exponentially increasing with the non-dimensional diameter.

The particle residence time from t_0 to t_2, namely, the ignition delay time was defined in Fig. 5.10 (a). After t_3 the emission started decreasing. The particle intensity further decreased to t_5, of which the intensity is the same as the ignition point at t_2. The thermal radiation intensity of the burning iron particle kept on falling with the particle cooling down till up t_6, and the thermal intensity suddenly increased at t_7. This phenomenon was also observed by Ning et al. [43, 65]. They explained that the supercooled molten O/Fe droplet solidified rapidly with fast latent heat release that heats the particle to the melting point. After the solidification process was completed, the particle would further cool down to the hot gas temperature.

5.1.2.4 *Particle temperature simulation and measurement*

In Paper XI, a novel model describing the single micron-sized iron particle combustion and phase change was introduced to understand the overall behavior of single iron particle combustion. This model contains five stages: solid-phase oxidation, melting, liquid-phase oxidation, cooling, and solidification (phase transition).

Fig. 5.10 (c) presents the simulated particle temperature under the same hot gas flow condition and following the same trajectory. A schematic illustration of different particle formed during the combustion is shown in Fig. 5.10 (d). Two distinct liquid phase compositions during the iron combustion are marked as L1 (liquid iron) and L2 (liquid oxides).

The inert heating of the cold particle starts right after the original iron particle enters the hot gas flow, until the particle temperature reaches over 700 K (from TGA experiments [66]). Solid-phase oxidation happens and particle status change from phase A to B as shown in Fig. 5.10 (c) and (d). Surface solid iron reacts with gaseous oxygen forming a thin outer layer of solid iron oxides that sticks to the particle. Particle temperature increases due to the released reaction heat and heat absorption from the surrounding hot gas flow until it reaches the melting point (s) of FeO.

Then, melting and phase change starts. It has been characterized by the tiny plateau region from both the intensity curve and temperature curve in Fig. 5.10 (a) and (c). For a single solid-liquid phase transition, the melting temperature should remain constant. However, there should be two plateaus in the melting process, including melting surface iron oxides (Phase B) and melting the remaining Fe in the particle (Phase C). These two melting points only have ~ 160 K different. In Phase B, FeO(s) form and soon disappears, accompanied by a rapid increase of L2 which is shown in the temporal evolution of the main solid and liquid mass fraction result in Paper

XI. However, this melting happens quickly, and the plateau is not direct evidence due to the very limited iron oxides compared with original iron.

The Liquid phase oxidation starts when L1 is formed, L1 reacts continuously with surrounding gas O_2 consumed to form L2 (Phase D). After the particle is entirely liquid, both thermal intensity and particle temperature increase dramatically, indicating an intense heat release in liquid-phase oxidation. After the fraction of L1 is consumed, particle temperature quickly rises to the peak point (Phase E) because the heat release is completed. The reaction stops and the particle cools down without any chemical reaction. Now the particle only consists of L2.

While cooling down, the cooling stage was characterized by Phase E into F. The particle loses heat to the surroundings and particle temperature drops. As the particle temperature decrease continuously to the melting temperature of Fe_3O_4, the solidification stage occurs. Herein the intensity jump (t_6-t_7) before the plateau (Phase F-G) is successfully identified in the model due to supercooled molten O/Fe droplet rapidly solidifying. Finally, the particle cools down as the solid iron oxide (Phase H) to gas temperature.

The particle surface shape changes from an irregular type to a sphere before melting from stage 1 to 5 according to the shape simulation result shown in Fig 5(d), which is consistent with the SEM sampling result shown in Fig. 5.19. The burning iron particle swelling is initially due to weight gain and then shrinks in the solidification stage due to increased particle density.

The five-stage model well reproduces the experimental results in Paper VIII. However, it should also be noticed that the real combustion process is much more complicated. The micro explosion and nano-size oxides released phenomena were observed in experiments while not considered in the current model.

This thesis implemented two-color imaging pyrometry for in-situ temperature measurement of biomass char particles and iron particles during combustion. In addition, the corresponding image processing and calibration procedures can be found in Paper VIII and Paper IX.

As a non-intrusive combustion diagnostic technique, two-color imaging pyrometry has been frequently applied in measuring particle temperatures, such as burning aluminum [67, 68], iron [46], magnesium [69], and biomass particles (Paper II). The surface temperature of the burning iron particle was determined by a two-color pyrometry technique [70]. In the two-color pyrometry, the ratio of the radiation intensities at two adjacent wavelengths could be related to the particle's surface temperature. According to Planck's law of radiation, the spectral emission intensity $E_{\lambda,T}$ is a function of emissivity ε_λ and temperature T:

$$E_{\lambda,T} = \frac{2\pi h c^2 \varepsilon_\lambda}{\lambda^5 [\exp(\frac{hc}{\lambda k T_p}) - 1]} \qquad (5.3)$$

where h is Planck's constant, c is the speed of light, k is the Boltzmann constant, and λ is the emission wavelength, ε_λ is the emissivity of the solid surface at an adjacent wavelength. When using two cameras equipped with two band-pass filters respectively to record the signal of the particle emission, the relation between particle emissions (E_λ), and the recorded signal intensities (I_λ) can be described as:

$$I = I_\lambda - I_{bkg} = \xi \int_0^\infty a_\lambda E_{\lambda,T} d\lambda \approx \xi a_\lambda E_{\lambda,T} \Delta\lambda \tag{5.4}$$

In which ξ is the exposure time of the cameras, I_{bkg} is the background intensity, a_λ is introduced as a system response efficiency factor, which can be obtained through calibration.

Therefore, according to Eq. (5.3) and Eq. (5.4), Particle temperature can be determined by:

$$\frac{I_1}{I_2} = \frac{a_{\lambda 1}\Delta\lambda_1}{a_{\lambda 2}\Delta\lambda_2} \left(\frac{\lambda_2}{\lambda_1}\right)^5 \frac{\varepsilon_{\lambda 1}}{\varepsilon_{\lambda 2}} \exp\left[\frac{hc}{kT_p}\left(\frac{1}{\lambda_2} - \frac{1}{\lambda_1}\right)\right] \tag{5.5}$$

Since the chosen wavelengths were quite close to each other and the iron particle can be assumed as a grey body at adjacent wavelengths such that the emissivity was nearly the same ($\varepsilon_{\lambda 1}/\varepsilon_{\lambda 2} \approx 1$).

In order to solve Eq. (5.5), a table was established to represent the quantitative relationship between the recorded intensity ratio and the particle temperature. In this table, the temperature ranged from 500 K to 3500 K with an interval of 0.1 K. Thus, when applying two-color imaging pyrometry in iron particle combustion, the particle temperature can be determined by looking up the table with the measured intensity ratio.

To obtain the system response efficiency, an IES-1000 (Labsphere) tungsten halogen-based point light source with a correlated color temperature of 2950 K was used to obtain the ratio $a_{\lambda 1}/a_{\lambda 2}$ in the calibration process. The relation between the real emission intensity of the lamp and the recorded intensity of the camera can be quantified by:

$$\frac{I_{\lambda 1,recorded} - I_{bkg}}{I_{\lambda 2,recorded} - I_{bkg}} = \frac{a_{\lambda 1}}{a_{\lambda 2}} \cdot \frac{\Delta\lambda_1}{\Delta\lambda_2} \cdot \frac{I_{\lambda 1,real}}{I_{\lambda 2,real}} \tag{5.6}$$
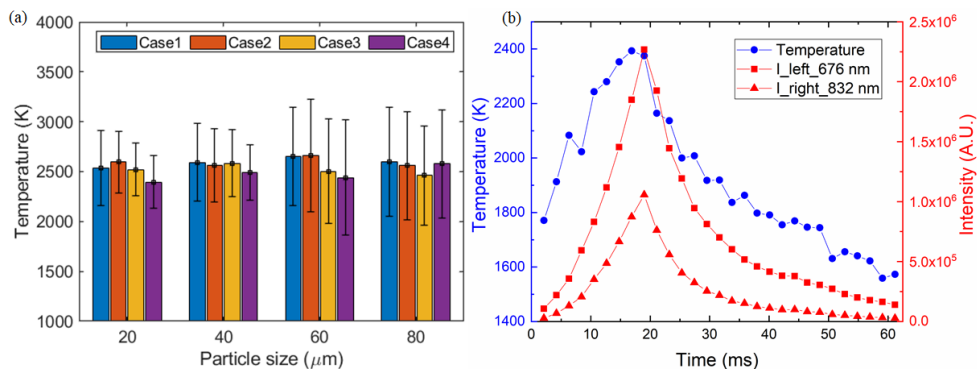
Figure 5.11: Particles mean temperature during the combustion of single iron particles as a function of the particle size at different oxygen concentrations (a). The error bars represent the standard derivations derived from over 200 particles. Temperature evaluation of single burning iron particle (80 μm) as a function of the residence time in flame case 1 (b).

The mean temperature of the combustion iron particles was derived from over 200 burning iron particles captured in the camera view, focusing on the height from 1 to 5 cm above the burner. There was a slight variance in mean temperatures regardless of particle sizes and oxygen concentration in the hot gas flow. The particles' mean temperature is much higher than the ambient flame temperature, which is ranged from 2396 K to 2660 K as shown in Fig. 5.11 (a). In Fig. 5.11 (b), one single iron particle (80 μm) burning temperature in flame case 1 was depicted with the captured particle thermal radiation through two bandpass filters. The temperature information was missing at the very beginning due to the low thermal radiation that the camera could hardly detect and missing at the end of the combustion process due to the limit of the camera vision.

5.2 Nanoparticles releasing and micro-explosion in burning micro-size iron particles

The central carrier gas for iron particles was switched from N_2 to CH_4 gas to study iron nanoparticle release and micro-explosion phenomena, where the micro-explosion is more often to be observed and nanoparticles releasing is more intense. A central CH_4 laminar jet diffusive flame is stabilized over the premixed flat pilot flame. The hot gas flow in the post-flame region was utilized to control the combustion condition of iron particles. In this measurement, a small amount of methane (0.45 l/min) was used to transport iron particles. Stereoscopic imaging techniques were applied to measure the 3D particle fields using several projections from different perspectives, which requires careful spatial calibration. The detailed procedure can be found in Paper IX and Paper X. Two high-speed cameras in stereo

40

configuration allowed 3D position and 3D velocity measurements of burning iron particles as well as 3D evaluation of particle microexplosions. Microexplosive processes are essential since it can affect both combustion stability and the formation of product components.
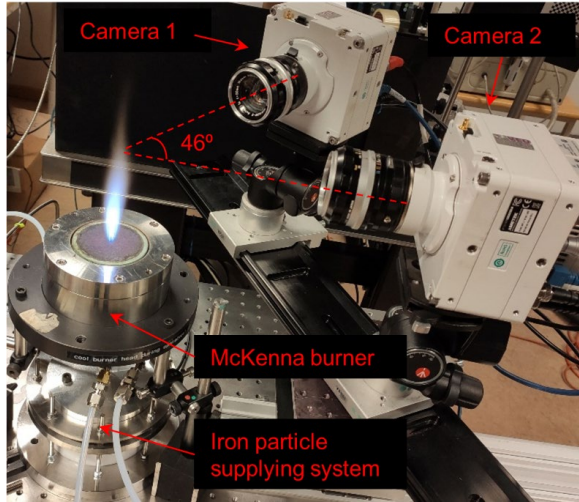

Figure. 5.12: Experimental setup for stereo imaging with two high-speed cameras and the iron particle combustion system.

5.2.1 Nanoparticles release

A release phenomenon was frequently observed during the iron particle combustion using magnified thermal radiation imaging and high-speed shadowgraphy. This release phenomenon was indirectly confirmed by observing the sampled combustion products with scanning electron microscopy (SEM), revealing multiple cracked particle shells and hollow structures.
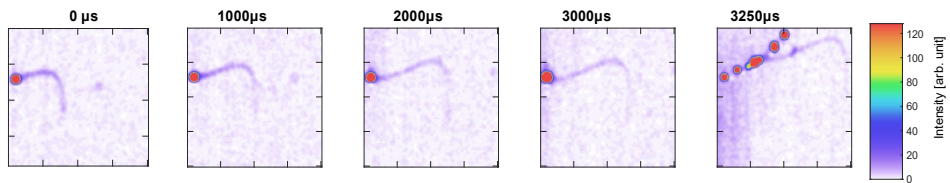

Figure 5.13: Shadowgraph sequence of particle release shadow over a duration of 4000µs in flame case 1(O_2 40%). At the end of the sequence, the darker left part is an artifact due to the release shadow being close to the noise level.
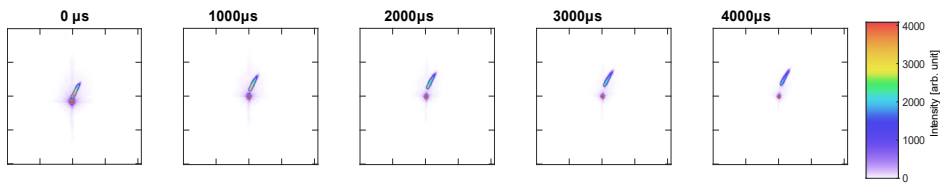
Figure 5.14: Image sequence of particle release over a duration of 4000µs in flame case 1, the image is overexposed to allow for better imaging of the release cloud location.

Fig. 5.13 shows shadowgraph sequences of simultaneous thermal radiation of a single iron particle terminated with an explosion, where the release phenomenon is shown in thermal radiation images. A similar luminous release trail has been presented in the thermal image sequence in Fig. 5.14. This highlights the fact that this release phenomenon is not always shown in thermal radiation images.

The release is believed to be caused as particle temperature increases after injection into the flame, yielding surface reactions with surrounding oxygen. When the temperature reaches the melting point of iron, the particle melts and becomes fully liquified. The ongoing reaction between iron and dissolved oxidizing gas on the liquid iron surface further increases particle temperature until it reaches its maximum, where most particle microexplosions happen [71]. During this temperature increase, some burning iron particle surface temperatures could reach the boiling temperature of the iron-oxides, allowing evaporation of liquid iron-oxides. Fig. 5.15 shows a shadowgraph image of a burning iron particle with a long release trail, indicating that the process may result in large amounts of nanoparticles formed.
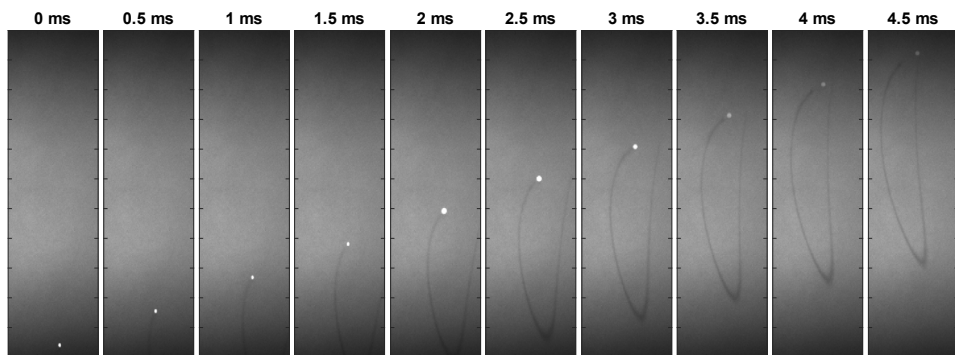

Figure 5.15: Shadowgraph image sequence of a single burning iron particle and its release trail for 4.5 ms. The dark sections in the top and bottom of each image are due to the limitations of laser light.

42

5.2.2 Micro-explosion

During the combustion of micron-sized iron powder, it is common to observe the micro-explosion behavior [71-73]. This kind of explosion in the combustion process is generally manifested as the nonlinear change of iron powder trajectory and the formation of smaller fragments. A similar phenomenon happens when burning aluminum and titanium particles [74, 75].

The observed microexplosions happened before particle extinction resulting in the change in trajectories, velocities, radiation intensities and fragmentation into smaller particles. It was observed for the first time that fragments of these microexplosions tend to produce planar structures, as shown in the last frame in Fig 5.13 and Fig. 5.16.
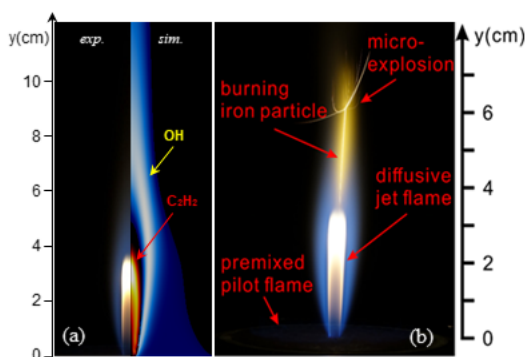

Figure 5.16: Profile of methane flames from experiments and simulations in flame case 1 with 40% O_2 left (a), and flame image illustration with particle explosion (b).

To further understand the iron flame, optical emission spectra have been captured and shown in Fig. 5.17. The formation of vapor phase iron-monoxides (FeO) at high temperatures was identified from the emission spectra. The molecular bands in the range of 550 - 650 nm are mainly attributed to the electronic transitions of FeO and specific spectral features are marked at 566, 590, 605 and 622 nm. The identified FeO spectrum aligns well with other experimental works [76, 77]. Note that the most intense peak at 590 nm is a combination of FeO and Na emission, most likely originating from impurities in the iron particles. The strong and clear FeO emission spectrum lines captured can originate from the evaporation of phase B of FeO.
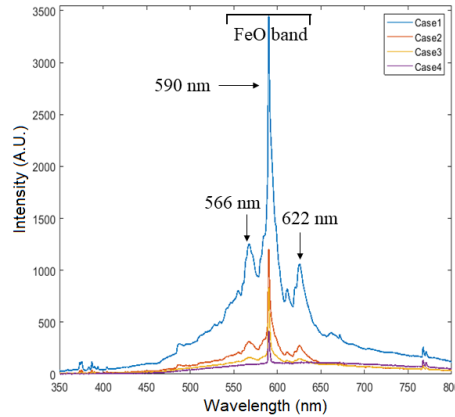
Figure 5.17: Emission spectra of burning iron particles in different flame cases.

During the micro-explosion process, the 3D motion of a single particle and the corresponding fragments were reconstructed using the stereo imaging technique. Before the micro-explosion, the single particle had a stable velocity of 2~3 m/s, which was comparable to the gas flow. However, after the micro-explosion, the velocities of most fragments increased to 2~6 times in very short time (~0.2 ms). Although the fragment velocities increased inconsistently, there is a trend that the higher oxygen concentration could lead to a faster fragment velocity. The reconstructed 3D motions suggest that a large inner pressure was generated and accumulated inside the particle during its rapid combustion process. After reaching a certain threshold, the inner pressure violently forced the burning particle apart. Then, due to the gravity and air resistance, the velocity of the fragments gradually decreased to follow the gas flow. In addition, multiple microexplosions showed a tendency to produce a planar explosion structure as seen by the two perspectives in Fig. 5.18. This planar explosion tendency could also be hinted from high-speed shadowgrahpy measurements such as the one seen in the last image of Fig. 5.13. Most microexplosions occurred around the maximum particle temperature, where the particle is a droplet consisting of a liquid iron core in conjunction with a liquid iron-oxides shell. When the temperature increases sharply, it tends to generate tangential stress and any built-up tension becomes more likely to release planarly, possibly creating a line-shaped tear releasing fragments into a plane.
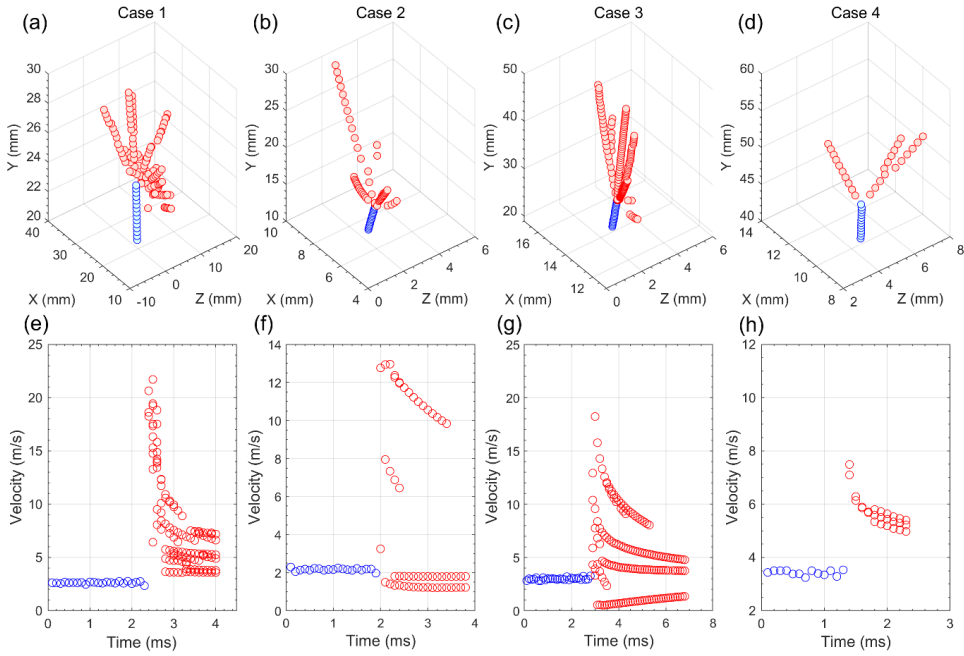
Figure 5.18: 3D motion of the single particle (blue dots) and the corresponding fragments (red dots) before and after the micro-explosion, respectively. (a-d): the reconstructed 3D particle paths. (e-h): the temporal evolutions of the particle 3D velocities.

In Paper IX, the probability and position of the micro-explosions are statistically studied. It is found that the oxygen concentration has a significant impact on the micro-explosion. Regarding the mechanism governing the micro-explosion of burning iron particles, the generation and expansion of gaseous bubbles inside the particle directly lead to a rapid increase in internal pressure, and finally fragment the particle into small pieces. There are three types of potential sources of the gas inside the particles: 1) the physical diffusion and dissolution of the surrounding gas flow [72, 78, 79]; 2) the vaporization of metal or metal oxides due to high particle temperature [80]; 3) the gas generated from certain chemical reactions inside the burning particles [72, 81, 82]. In addition, the gas expansion is associated with the surrounding gas temperature and oxygen concentration, where the gradients play an important role in the micro-explosion. Generally, since the micro-explosions will dramatically affect the key combustion characteristics of the particles, a comprehensive understanding of the mechanism will help control the micro-explosion of iron particle combustion in practical applications.

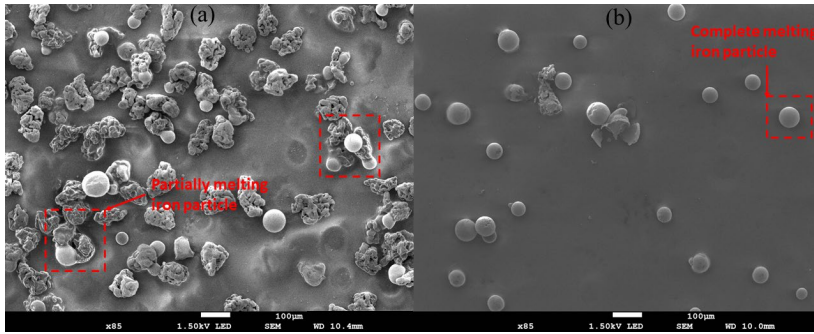### 5.2.3 Particle sampling and morphology analyze

Figure 5.19: SEM images of burning iron particles collected by impact copper plate at HAB = 100 mm (a), and at HAB = 200 mm (b) in flame case 1.

In Fig. 5.19, particle samples collected at HAB = 100 mm consisted of a mixture of raw-looking and spherical particles. Most interesting is that the shapes of the combination highly existed, representing the intermediate combustion product generated in the ignition delay period. The particle samples collected at HAB = 200 mm (around t_3) mostly consist of spherical combust products of the iron oxides. In Fig. 5.20, it could be found that a large amount of floc-like sub-micron particles were generated and agglomerated at the reacting particle surface and the impact tape, which was direct evidence of forming nanoparticles during burning single iron particles. There were no significant visual differences observed on the micrographs between these two different single iron particles in Fig. 5.20 (a) and (b). The released phenomena observed above, which were also predicted by thermodynamic equilibrium calculations in Henrik's work [83], indicated that nanoparticles formed when gaseous in the form of Fe (g) or FeO (g) reacts with the surrounding oxidizers. This fume mainly consisted of aggregates of nanosized iron oxide in the form of α-Fe_2O_3 and β-Fe_2O_3 [46, 83].
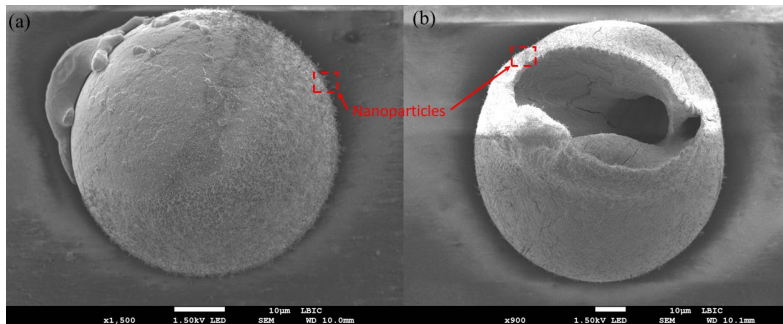

Figure 5.20: SEM image of two typical combust samples collected by the impact plate in flame case 1 at HAB = 150 mm (a) and HAB = 250 mm (b).

Figure 5.21: SEM image of combust particles collected by sampling mesh at HAB = 450 mm in flame case 1 (a) and case 3 (b).

Fig. 5.21 shows the combust particles collected at the end of the quartz tube in flame case 1 and case 3. Most of the combust iron particles are spherical with a hollow structure. The particle size distributions of the combust products have been statistically investigated and the results are summarized in Fig. 5.22.
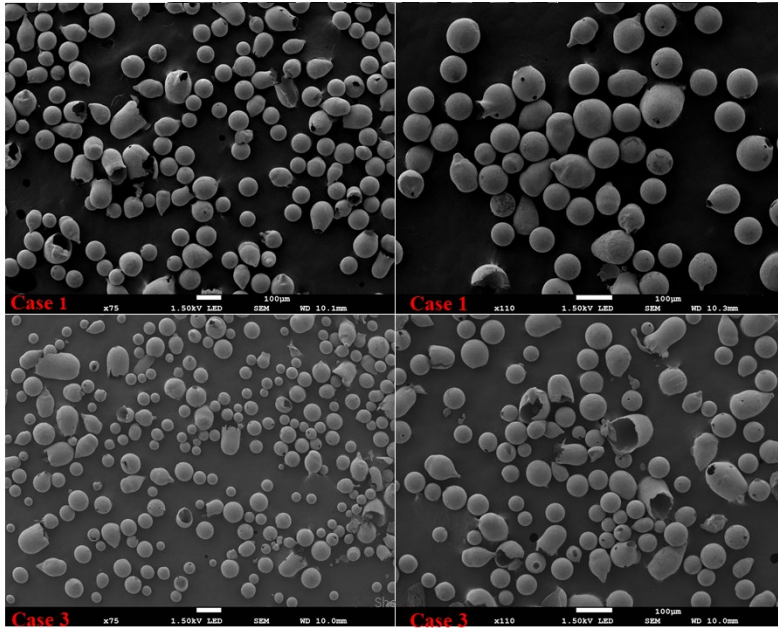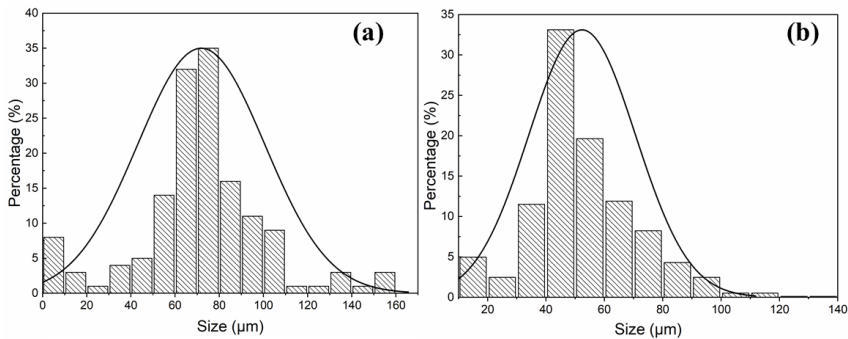

Figure 5.22: The size distribution of combust particles collected by sampling mesh at HAB = 450 mm in flame case 1 (a) and case 3 (b).

The combustion products had a mean size diameter of around 80 μm in case 1, and around 50 μm for the samples in case 3. The sampled combust particles had a similar size as the raw iron particles in case 1. However, the sampled particles in case 3 significantly shrink compared to the raw iron particles. As seen, the combustion environment strongly influenced the collected sample size. Flame case 1 had the highest oxygen concentration (vol. 40%) in the combustion products, leading to the most intense Fe-O reaction and a more significant iron particle oxidization rate. In flame case 1, there was a faster pressure build-up process inside the shell than in other cases, which finally led to a larger iron-oxide shell than in case 3. Despite the similar size of the combust particles as the raw iron particles had been detected in flame case 1, most of the structure of the combust particles were hollow with very thin shells of several micrometers, as shown in Fig. 5.23. It could lead to an iron mass loss in flame case 1, which would be more significant in case 3. As discussed above, the dramatic size shrinking observed in case 3 was directly related to the nanoparticles release. Most of the iron-oxides nanoparticles formed from the vaporized iron/iron-oxides during the combustion. The nanoparticles release would finally result in a certain iron mass loss in the repeating metal cycle loop. To reduce the formed nanoparticles (iron mass loss), a higher excess of oxygen concentration in a lower temperature flame condition would help suppress the formation of the nanoparticles. The optimal trajectory, the balance between oxygen concentration and hot gas products temperature, needs further study to limit the formation of released nanoparticles.
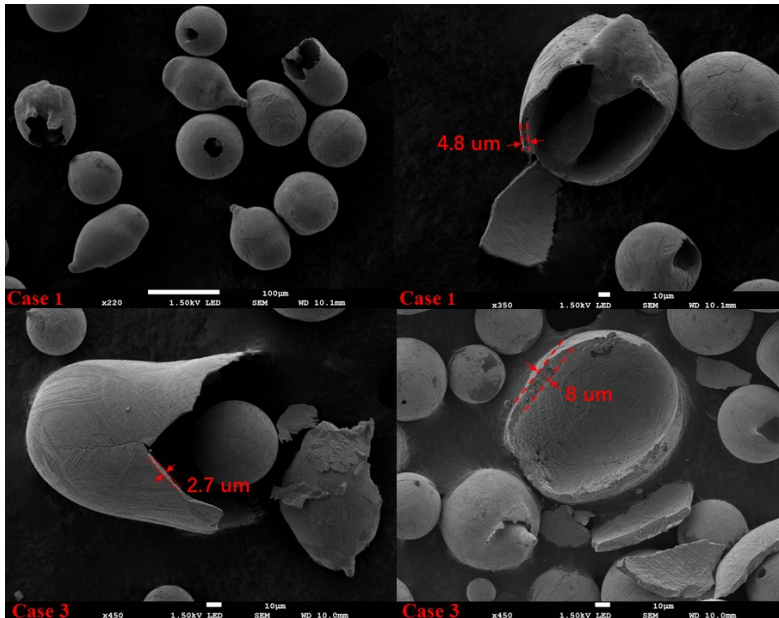

Figure 5.23 Some typical combust particles by sample-collecting mesh at HAB = 450 mm at higher magnifications.

6 Summary and outlook

6.1 Summary

This thesis has been focused on a deepened understanding and control of the combustion process of biomass and metal fuels, using these alternative solid fuels to substitute fossil fuels to cut CO_2 emissions.

In the first part, the temporal variation of the surface temperature and volatile gas temperature of individually burning biomass pellets was derived using phosphor thermometry and two-line atomic fluorescence thermometry. The spatial distribution of the PAH in the volatile gas was recorded by two-dimensional laser-induced fluorescence. The PAH in the volatile gases is mainly distributed close to the surface of the pellets before being consumed downstream. The surface temperature significantly increased during the char conversion but was still ~500 K lower than the hot gas environment.

A preliminary investigation of the potassium release process for biomass char particles using LIPF imaging was conducted to provide spatially resolved information on the dominant species of KCl and KOH that formed during the char oxidation period. A laminar multi-jet burner was designed to provide uniform hot gas environments to calibrate the gas-phase KOH and KCl, in which a homogenous temperatures distribution ranging from 1000 to 2000 K are provided. For the first time, the release of potassium from single burning pulverized wheat straw char particle was quantitatively identified. Absorption spectroscopy techniques are applied for quantitative measurement of key species, such as the concentrations of KOH and KCl. Based on the calibration, the KOH/KCl distribution surrounding the burning char particles was derived, revealing the potassium release process during the char oxidation period. The results show that the potassium release rate is almost constant during the char oxidation process from 10 to 70 ms, and over 60% of the total potassium is in the form of KOH.

In the second part, an advanced metal powder combustion system was designed and tested. The seeding apparatus can provide a stable seeding concentration of particles depending on the size and density of the particle. This seeding system can provide even and steady particle gas flow for around 1 minute for iron particles.

Inspired by clustering algorithms, a clustering-based particle detection (CBPD) method was proposed for digital holography (DH) for particle detection. This data-

driven method features automatic recognition of particles, particle edges, background, and accurate separation of overlapping particles. Based on the CBPD method, a versatile high-speed digital in-line holography (DIH) is employed to reconstruct the 3D particle field and simultaneously quantify the size, 3D location and velocity of burning iron particles in a well-controlled methane/air premixed Bunsen flame.

With successfully automatic recognition and separation of overlapping iron particles from the flame images, the single iron particle combustion in a well-controlled laminar premixed flame with a modified Mckenna flat-flame burner through advanced optical diagnostic techniques was investigated. With two high-speed cameras operating at 10,000 frames per second, the 3D motion and mean surface temperature of burning iron particles during the micro-explosion process were measured using stereo imaging and two-color pyrometry, respectively. An important phenomenon of nano-sized iron-oxide particles released during the combustion of iron particles has been identified. Micro-explosion of burning iron particles was observed during the combustion process, which is complex and can affect both combustion stability and the formation of product components. The morphology of raw iron particles and the combust products collected by sampling meshes have been analyzed by scanning electron microscopy (SEM).

6.2 Outlook

Based on the techniques and results developed in the thesis, a similar methodology can be extended to study other solid fuels such as aluminum and metal alloys. In addition, plasma/microwave could assist the metal combustion. All discussions in this thesis are limited to laminar flames and future studies of turbulent flames are expected. Several ongoing and future works are presented:

A. Identification of flame fronts in a laminar flame using PLIF and TLAF thermometry

Tang et al. [44] had found that the apparent flame front was detectable when the particle concentration was above a critical value. However, the thermal and chemical properties of this apparent flame front are not yet well understood. To reveal this fundamental issue, the particle temperature and the local gas temperature and species profiles can be visualized and compared near the apparent flame front. PLIF technique can be used to image the species distribution and the TLAF can be applied for gas temperature measurement. To reduce the multiple scattering interference, the SLIPI (Structured Laser Illumination Planar Imaging) technique can be adopted.

B. PLIF measurement of FeO/AlO and atomic Fe/Al

The PLIF technique can be employed for AlO and atomic Al mapping in Al flame and FeO and atomic Fe mapping in Fe flame. In detail, AlO LIF can be excited from the blue-green $(X^2\Sigma^+-B^2\Sigma^+)$ band systems using a Nd:YAG-pumped dye laser tuned to near 465nm. An optical parametric oscillator (OPO) pumped by a pulsed Nd:YAG laser can be tuned to 308.2nm and 559.5nm for Al-LIF and FeO-LIF detections, respectively. The KrF excimer can be tuned to 248nm for Fe-LIF detection. Owing to the possible vapor-phase combustion mode of aluminum, atomic Al density should be high near the Al particle. In contrast, the atomic iron density will be much lower near the Fe particle because the primary combustion is in heterogeneous combustion mode.

C. Flame front propagation and response to turbulence

After identifying characteristic scalars for the flame front, the metal flame at varying turbulence intensities can be visualized using the PLIF technique. Phenomenons such as the flame front propagation, stretching, wrinkling, broadening, local extinction and re-ignition can hopefully be captured. Mechanisms of extinction and re-ignition can be analyzed using a previously proposed single-particle ignition and combustion model. High-spatial-resolved detections near the flame front will be carried out to clarify the impacts of local particle interactions on flame propagations.

This proposed project is based on experiments performed in laminar combustion configurations for burning single iron particles. The results will provide urgently needed data for CFD simulation and later modeling validation. In recent years, many studies have been performed on metal fuel particle combustion, but most of these studies are limited to single particles or particle clouds combustion under laminar conditions. Turbulent environments exist in most practical applications. To the best of our knowledge, the combustion characteristics of single iron particle/particle clouds under such environments have not been established or studied.

The global flame properties will be influenced by the microscopic scales of local flame properties in the turbulent flame. The relation between the local and global flame properties is essential for modeling complex two-phase combustion and helping improve new burner designs for practical industrial applications. According to previous studies [84, 85], the burning time of metal particles can be reduced in turbulent environments since the turbulent flow enhances the heat and mass transfer between the fuel droplet and the hot oxidizing gas flow. For the coal particle group combustion, it is proved that turbulence strongly impacts particle ignition distance [86] and particle cloud jet flame structure [87]. However, such studies are blank in iron particle combustion.

The proposed experiments can be performed both in a small lab-scale turbulent premixed jet flame (LUPJ burner shown in Fig. 6.1 (a)) and a large-scale Bunsen flame (DRZ burner shown in Fig 6.1 (c)) with different turbulent levels.
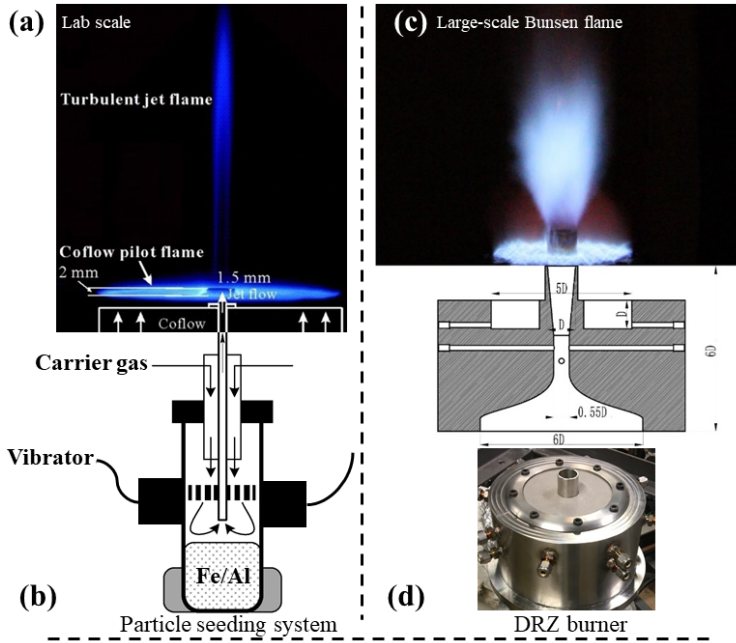
Figure 6.1: Image of turbulent premixed jet flame in a lab-scale LUPJ burner (a), schematic of the iron particles system (b), a large-scale Bunsen flame from a DRZ burner (c), and image of DRZ burner (d).

The iron particles can be ignited and burnt in the post-flame environment supported by a premixed flat flame burner. Using multiple optical measurement methods, the flame structure of the iron-particles jet flame under different turbulent conditions can be studied.

D.   Metal flame temperature measurement using LITGS

Flame temperature with and without iron particles (40 μm) at 2 cm and 4 cm above the McKenna burner were measured (flame conditions in Paper VIII) using laser-induced thermal grating spectroscopy (LITGS) [88]. The flame temperature measurements with iron particles seeding at 2 cm height above burner (HAB) show a lower flame temperature (~20 K) than without seeding in case 1. It is because the particle is somehow in the preheating process (ignition delay period) and the particle absorbs more heat from the flame than the heat released from surface reaction (oxidation). In contrast, in the measurement at 4 cm HAB, we see ~70 K higher temperature with the metal seeding than without it, in which the particle is in accelerating combustion period with violent oxidation reaction that the heat transfer and radiation from burning particles heat the surrounding gas.

However, the LITGS signal is strongly influenced by the metal particle seeding concentration due to breakdown and scattering. For testing the limit of applying LITGS in the metal flame, the in-situ high-speed DIH was used to measure the

particle number density in the LITGS probe volume. For example, with a power supply at 5.25 KV, the particle number density is $2/cm^3$ at 2 cm HAB, and $1/cm^3$ at 4 cm HAB. Thus, LITGS is suitable for single or low concentrations of metal particle seeding. As discussed, TLAF will be adopted for higher metal particle concentration in the flame front study. More experiments will be carried out in the future.

E. Pollutant emission detection

Using a Nd:YAG laser pumped dye laser, NO PLIF can be conducted to map its profile around burning particles. Since the particle temperature will be higher than the surroundings, the NO concentration is possibly significant close to the particle surface. This speculation needs to be testified through a high-spatially-resolved detection approach. Furthermore, the equivalence ratio, the co-flow temperature, and the flow rate can be varied to study their effects on NO formation to control NO_X emission.

References

1. IEA, *Global Energy and CO₂ Status Report 2018 https://www.iea.org/reports/global-energy-co2-status-report-2019.* INTERNATIONAL ENERGY AGENCY, 2018.
2. Schiermeier, Q., et al., *Energy alternatives: Electricity without carbon.* Nature, 2008. **454**(7206): p. 816-823.
3. Bergthorson, J.M., *Recyclable metal fuels for clean and compact zero-carbon power.* Progress in Energy and Combustion Science, 2018. **68**: p. 169-196.
4. Chen, H., et al., *Progress in electrical energy storage system: A critical review.* Progress in Natural Science, 2009. **19**(3): p. 291-312.
5. Rosen, M.A. and S. Koohi-Fayegh, *The prospects for hydrogen as an energy carrier: an overview of hydrogen energy and hydrogen energy systems.* Energy, Ecology and Environment, 2016. **1**(1): p. 10-29.
6. Dreizin, E.L., *Metal-based reactive nanomaterials.* Progress in Energy and Combustion Science, 2009. **35**(2): p. 141-167.
7. Shkolnikov, E.I., A.Z. Zhuk, and M.S. Vlaskin, *Aluminum as energy carrier: Feasibility analysis and current technologies overview.* Renewable and Sustainable Energy Reviews, 2011. **15**(9): p. 4611-4623.
8. Beach, D.B., et al., *Solid-State Combustion of Metallic Nanoparticles: New Possibilities for an Alternative Energy Carrier.* Journal of Energy Resources Technology, 2006. **129**(1): p. 29-32.
9. Rosenband, V., *Thermo-mechanical aspects of the heterogeneous ignition of metals.* Combustion and Flame, 2004. **137**(3): p. 366-375.
10. Aldén, M., et al., *Visualization and understanding of combustion processes using spatially and temporally resolved laser diagnostic techniques.* Proceedings of the Combustion Institute, 2011. **33**(1): p. 69-97.
11. Eckbreth, A.C., *Laser Diagnostics for Combustion Temperature and Species (1st ed.).* 1996, London: CRC Press.
12. Lee, J., et al., *Laser-induced breakdown thermometry via time-of-arrival measurements of associated acoustic waves.* Applied Physics Letters, 2018. **113**(12): p. 123504.
13. Lee, J., et al., *Thermometry of combustion gases using light emission and acoustic wave from laser-induced sparks.* Journal of Physics D: Applied Physics, 2019. **52**(31): p. 315201.

14. Katz, J. and J. Sheng, *Applications of Holography in Fluid Mechanics and Particle Dynamics.* Annual Review of Fluid Mechanics, 2010. **42**(1): p. 531-555.
15. Schnars, U. and W. Jueptner, *Hologram Recording, Numerical Reconstruction, and Related Techniques*. 2005, Springer, Berlin.
16. Schnars, U., et al., *Digital holography*, in *Digital Holography and Wavefront Sensing*. 2015, Springer. p. 39-68.
17. Malkiel, E., et al., *The three-dimensional flow field generated by a feeding calanoid copepod measured using digital holography.* 2003. **206**(20): p. 3657-3666.
18. Allano, D., et al., *Three-dimensional velocity near-wall measurements by digital in-line holography: calibration and results.* Applied Optics, 2013. **52**(1): p. A9-A17.
19. Guildenbecher, D.R., et al., *Accurate measurement of out-of-plane particle displacement from the cross correlation of sequential digital in-line holograms.* Opt Lett, 2013. **38**(20): p. 4015-4018.
20. Guildenbecher, D.R., M.A. Cooper, and P.E.J.A.O. Sojka, *High-speed (20kHz) digital in-line holography for transient particle tracking and sizing in multiphase flows.* **55**(11): p. 2892.
21. Guildenbecher, D.R., et al., *Quantitative, three-dimensional imaging of aluminum drop combustion in solid propellant plumes via digital in-line holography.* 2014. **39**(17): p. 5126-5129.
22. Chen, Y., et al., *Study of aluminum particle combustion in solid propellant plumes using digital in-line holography and imaging pyrometry.* 2017. **182**: p. 225-237.
23. Karim, G.A., *Fuels, Energy, and the Environment*. 1st Edition ed. 2012: CRC Press.
24. G. Miller, B., *Combustion Engineering Issues for Solid Fuel Systems*. 2008: Academic Press.
25. Weng, W., et al., *A novel multi-jet burner for hot flue gases of wide range of temperatures and compositions for optical diagnostics of solid fuels gasification/combustion.* Rev Sci Instrum, 2017. **88**(4): p. 045104.
26. Borggren, J., et al., *Diode laser-based thermometry using two-line atomic fluorescence of indium and gallium.* Applied Physics B, 2017. **123**(12): p. 278.
27. Colver, G.M., S.W. Kim, and T.-U. Yu, *An electrostatic suspension method for testing spark breakdown, ignition, and quenching of powders.* Journal of Electrostatics, 1996. **37**(3): p. 151-172.
28. Shoshin, Y. and E. Dreizin, *Production of Well-Controlled Laminar Aerosol Jets and Their Application for Studying Aerosol Combustion Processes.* Aerosol Science and Technology, 2002. **36**(9): p. 953-962.
29. Shoshin, Y. and E. Dreizin, *Particle combustion rates in premixed flames of polydisperse metal—air aerosols.* Combustion and Flame, 2003. **133**(3): p. 275-287.

30. Shoshin, Y. and E.L. Dreizin, *Laminar Lifted Flame Speed Measurements for Aerosols of Metals and Mechanical Alloys.* AIAA Journal, 2004. **42**(7): p. 1416-1426.
31. Gill, R.J., S. Mohan, and E.L. Dreizin, *Sizing and burn time measurements of micron-sized metal powders.* Rev Sci Instrum, 2009. **80**(6): p. 064101.
32. Nada, F.A., et al., *Development of an automatic routine for calibration of thermographic phosphors.* Measurement Science and Technology, 2014. **25**(2): p. 025201.
33. Ciajolo, A., A. D'Anna, and R. Barbella, *PAH and high molecular weight species formed in a premixed methane flame.* Combustion Science and Technology, 1994. **100**(1-6): p. 271-281.
34. Simões, G., et al., *Effect of gas temperature and oxygen concentration on single particle ignition behavior of biomass fuels.* Proceedings of the Combustion Institute, 2017. **36**(2): p. 2235-2242.
35. Weng, W., et al., *Temporally and spectrally resolved images of single burning pulverized wheat straw particles.* Fuel, 2018. **224**: p. 434-441.
36. Weng, W., et al., *Single particle ignition and combustion of pulverized pine wood, wheat straw, rice husk and grape pomace.* Proceedings of the Combustion Institute, 2019. **37**(3): p. 2663-2671.
37. Weng, W., et al., *Spectrally resolved ultraviolet (UV) absorption cross-sections of alkali hydroxides and chlorides measured in hot flue gases.* Applied Spectroscopy, 2018. **72**(9): p. 1388-1395.
38. Weng, W., et al., *Quantitative measurement of atomic potassium in plumes over burning solid fuels using infrared-diode laser spectroscopy.* Energy and Fuels, 2017. **31**(3): p. 2831-2837.
39. Fatehi, H., et al., *Numerical simulation of ignition mode and ignition delay time of pulverized biomass particles.* Combustion and Flame, 2019. **206**: p. 400-410.
40. Weng, W., et al., *Optical measurements of KOH, KCl and K for quantitative K-Cl chemistry in thermochemical conversion processes.* Fuel, 2020. **271**: p. 117643.
41. Goroshin, S., et al., *Optical Pyrometry of Fireballs of Metalized Explosives.* Propellants, Explosives, Pyrotechnics, 2006. **31**(3): p. 169-181.
42. Makino, A., *Fundamental aspects of the heterogeneous flame in the self-propagating high-temperature synthesis (SHS) process.* Progress in Energy and Combustion Science, 2001. **27**(1): p. 1-74.
43. Ning, D., et al., *Burn time and combustion regime of laser-ignited single iron particle.* Combustion and Flame, 2021. **230**(111424): p. 111424.
44. Tang, F.-D., et al., *Flame propagation and quenching in iron dust clouds.* Proceedings of the Combustion Institute, 2009. **32**(2): p. 1905-1912.
45. Alex W, S.G., Andrew H, *An Attempt to Observe the Discrete Flame Propagation Regime in Aluminum Dust Clouds.* 25th ICDERS, 2015.
46. Tóth, P., et al., *Combustion behavior of pulverized sponge iron as a recyclable electrofuel.* Powder Technology, 2020. **373**: p. 210-219.

47. Julien, P., et al., *Freely-propagating flames in aluminum dust clouds.* Combustion and Flame, 2015. **162**(11): p. 4241-4253.

48. Julien, P., et al., *Flame structure and particle-combustion regimes in premixed methane–iron–air suspensions.* Proceedings of the Combustion Institute, 2015. **35**(2): p. 2431-2438.

49. Bergthorson, J.M., et al., *Direct combustion of recyclable metal fuels for zero-carbon heat and power.* Applied Energy, 2015. **160**: p. 368-382.

50. Soo, M., et al., *Reaction of a Particle Suspension in a Rapidly-Heated Oxidizing Gas.* Propellants, Explosives, Pyrotechnics, 2015. **40**(4): p. 604-612.

51. Bergthorson, J.M., et al., *Metal-water combustion for clean propulsion and power generation.* Applied Energy, 2017. **186**: p. 13-27.

52. Soo, M., et al., *Combustion of particles, agglomerates, and suspensions – A basic thermophysical analysis.* Combustion and Flame, 2018. **192**: p. 384-400.

53. McRae, M., et al., *Stabilized, flat iron flames on a hot counterflow burner.* Proceedings of the Combustion Institute, 2019. **37**(3): p. 3185-3191.

54. Zeldovich, I.B., et al., *Mathematical theory of combustion and explosions*. 1985, United States: Consultants Bureau,New York, NY. Medium: X; Size: Pages: 618 2008-2002-2007.

55. Tinevez, J.Y., *simpletracker (https://github.com/tinevez/simpletracker)*. 2020, GitHub.

56. Settles, G.S. and M.J. Hargather, *A review of recent developments in schlieren and shadowgraph techniques.* Measurement Science and Technology, 2017. **28**(4): p. 042001.

57. Huang, J., et al., *Recent advances and applications of digital holography in multiphase reactive/nonreactive flows: a review.* Measurement Science and Technology, 2021. **33**(2): p. 022001.

58. Li, H., et al., *In-lab in-line digital holography for cloud particle measurement experiment*, in *Hyperspectral Remote Sensing Applications and Environmental Monitoring and Safety Testing Technology*. 2016.

59. Kanungo, T., et al., *An efficient k-means clustering algorithm: Analysis and implementation.* IEEE transactions on pattern analysis machine intelligence, 2002. **24**(7): p. 881-892.

60. Ester, M., et al. *Density-based spatial clustering of applications with noise*. in *Int. Conf. Knowledge Discovery and Data Mining*. 1996.

61. Glassman, I., *Metal combustion processes*. 1959, PRINCETON UNIV NJ JAMES FORRESTAL RESEARCH CENTER.

62. Glassman, I., R.A. Yetter, and N.G. Glumac, *Combustion*. 2014: Academic press.

63. Wright, A., S. Goroshin, and A.J. Higgins. *Combustion Time and Ignition Temperature of Iron Particles in Different Oxidizing Environments*. in *Proceedings of the 25th International Colloquium on the Dynamics of Explosions and Reactive Systems*. 2015. Leeds, UK.

64. Tang, F.-D., S. Goroshin, and A.J. Higgins, *Modes of particle combustion in iron dust flames.* Proceedings of the Combustion Institute, 2011. **33**(2): p. 1975-1982.

65. Ning, D., et al., *Temperature and phase transitions of laser-ignited single iron particle.* Combustion and Flame, 2022. **236**: p. 111801.

66. Schiemann, M., *Iron particles as carbon-neutral fuel in spray roasting reactors*, in *Conference: 8th European Combustion Meeting*. 2017: Dubrovnik, Croatia. p. 487-492.

67. Feng, Y., et al., *Effect of ambient temperature on the ignition and combustion process of single aluminium particles.* Energy, 2018. **162**: p. 618-629.

68. Chen, Y., et al., *Study of aluminum particle combustion in solid propellant plumes using digital in-line holography and imaging pyrometry.* Combustion and Flame, 2017. **182**: p. 225-237.

69. Liu, X., M. Schoenitz, and E.L. Dreizin, *Combustion of Mg and composite Mg·S powders in different oxidizers.* Combustion and Flame, 2018. **195**: p. 292-302.

70. Guo, H., J.A. Castillo, and P.B. Sunderland, *Digital camera measurements of soot temperature and soot volume fraction in axisymmetric flames.* Applied Optics, 2013. **52**(33): p. 8040-8047.

71. Poletaev, N.I. and M.Y. Khlebnikova, *Combustion of Iron Particles Suspension in Laminar Premixed and Diffusion Flames.* Combustion Science and Technology, 2020: p. 1-22.

72. Li, Y.-H., et al., *Synergetic combustion behavior of aluminum and coal addition in hybrid iron-methane-air premixed flames.* Combustion and Flame, 2021. **228**: p. 364-374.

73. Wright, A., S. Goroshin, and A. Higgins. *Combustion time and ignition temperature of iron particles in different oxidizing environments*. in *25th International Colloquium on the Dynamics of Explosions and Reactive Systems*. 2015.

74. Dreizin, E.L., *Effect of Phase Changes on Metal-Particle Combustion Processes.* Combustion, Explosion and Shock Waves, 2003. **39**(6): p. 681-693.

75. Badiola, C. and E.L. Dreizin, *Combustion of micron-sized particles of titanium and zirconium.* Proceedings of the Combustion Institute, 2013. **34**(2): p. 2237-2243.

76. West, J.B. and H.P. Broida, *Chemiluminescence and photoluminescence of diatomic iron oxide.* The Journal of Chemical Physics, 1975. **62**(7): p. 2566-2574.

77. Toro, C., et al., *On the Detection of Spectral Emissions of Iron Oxides in Combustion Experiments of Pyrite Concentrates.* Sensors, 2020. **20**(5): p. 1284.

78. Badiola, C. and E.L.J.P.o.t.C.I. Dreizin, *Combustion of micron-sized particles of titanium and zirconium.* 2013. **34**(2): p. 2237-2243.

79. Wainwright, E.R., et al., *Viewing internal bubbling and microexplosions in combusting metal particles via x-ray phase contrast imaging.* Combustion and Flame, 2019. **199**: p. 194-203.

80. Tang, Y., et al., *Combustion of aluminum nanoparticle agglomerates: From mild oxidation to microexplosion.* Proceedings of the Combustion Institute, 2017. **36**(2): p. 2325-2332.

81. Dalke, T., J. Brink, and M. Weller, *Material determination using spark observation.* Global Journal of Engineering Education, 2013. **15**(3).

82. Stanmore, B.R., J.F. Brilhac, and P. Gilot, *The oxidation of soot: a review of experiments, mechanisms and models.* Carbon, 2001. **39**(15): p. 2247-2268.

83. Wiinikka, H., et al., *Pulverized Sponge Iron, a Zero-Carbon and Clean Substitute for Fossil Coal in Energy Applications.* Energy & Fuels, 2018. **32**(9): p. 9982-9989.

84. Zhang, J., et al., *Experimental study on aluminum particles combustion in a turbulent jet.* Energy, 2021. **214**.

85. Corcoran, A.L., V.K. Hoffmann, and E.L. Dreizin, *Aluminum particle combustion in turbulent flames.* Combustion and Flame, 2013. **160**(3): p. 718-724.

86. Xu, K., et al., *Experimental study on ignition behavior of pulverized coal particle clouds in a turbulent jet.* Fuel, 2016. **167**: p. 218-225.

87. Shen, H., et al., *Eulerian LES simulation of coal jet flame with a simplified DQMOM model.* Fuel, 2018. **216**: p. 475-483.

88. Hot, D., et al., *Mid-infrared laser-induced thermal grating spectroscopy of hot water lines for flame thermometry.* Proceedings of the Combustion Institute, 2021. **38**(1): p. 1885-1893.

Acknowledgements

Finally, my PhD thesis has been completed during the pandemic. Combustion physics, which means "燃烧物理" in mandarin. Coincidentally, there are also many fires "火" in my name as fate is already doomed. Turning myself from a material scientist to a combustion engineer is not an easy way to go, but I did it. Looking back on these years during my PhD study, it was a way full of twists and turns that will be the most memorable part of my life. As Nietzsche said, "What doesn't kill you makes you stronger." Other than the study, I like the living life in Lund, where I met many friends.

Firstly, I want to thank my principal supervisor, Prof. Zhongshan Li, who gives me the opportunity to conduct PhD in the Combustion Physics division. I could not find my potential skills without your supervision and encouragement. You told me about many things during our discussion these years, but nothing was more precious than your enthusiasm for pushing the boundaries of human knowledge. You can always give me enormous ideas to try and outline a complex experiment in simple and common words.

A great gratitude belongs to my co-supervisors, Prof. Marcus Aldén, for providing me the financial support during my PhD and helping with correcting my papers, thesis and other research activities. You acted as an academical role model to me. Your dedication, motivation, and enthusiasm for scientific research have always inspired me.

I am also grateful to the current head of the division, Prof. Per-Erik Bengtsson. Thanks for your time to talk and support when I met difficulties.

I would like to give a great thanks to Dr. Wubin Weng. Without your help and advice, it would be impossible for me to complete this thesis work. I appreciate the time we spend together in the Lab, office, and the daily life. You were always friendly and patient in helping me, and I learned a lot from you. I also want to express my gratitude to Prof. Edourad Berrocal, Prof. Xue-Song Bai, Prof. Mattias Richter, Prof. Chengdong Kong, Prof. Andreas Ehn, Dr. Christian Brackmann, and Dr. Yong Qian for your help with my research work in the division.

Many thanks should also be given to all those who have worked with me, David Scanned, Henrik Feuk, Dina Hot, Anna-Lena Sahlberg, Arman Subash, Yue Qiu,

Summary of papers

Paper I: Dual-laser-induced Breakdown Thermometry via Sound Speed Measurement: A New Procedure for Improved Spatiotemporal Resolution.

*<u>**S. Li**</u>, W. Weng, C. Kong, M. Aldén, Z. Li, Sensors 20 (2020) 2803.*

In this paper, the acoustic wave measurement from the laser-induced breakdown has been developed as gas thermometry in combustion atmospheres. Two laser-induced breakdown spots are generated and the local gas temperature between these two spots is determined through the measurement of the sound speed between them. We proposed a new measurement procedure, where two individual laser pulses with optimized firing order and delay time were employed. With the new measurement procedure, the system uncertainty caused by local gas breakdown can be largely avoided and furthermore, the temporal and spatial resolutions can reach up to 0.5 ms and 10 mm, respectively.

I planned the experiments. I conducted the measurements together with W. Weng. I analyzed all the data. I wrote the manuscript with some input from the other authors.

Paper II: Temporal temperature measurement on burning biomass pellets using phosphor thermometry and two-line atomic fluorescence.

*W. Weng, H. Feuk, <u>**S. Li**</u>, M. Richter, M. Aldén, Z. Li, Proceedings of the Combustion Institute 38 (2021) 3949-3958.*

In this paper, accurate in-situ optical measurements of surface temperature, volatile gas temperature, and polycyclic aromatic hydrocarbon (PAH) emission over the whole burning history of individual biomass pellets in various combustion atmospheres have been detailed studied. Two biomass fuels, the wood and straw pellets, were burned in a well-controlled combustion atmosphere provided by a laminar flame burner. The temperature range is from 1390 K to 1840 K, and the oxygen concentration is from 0 to 4.5%. It is the first time that the surface temperature of burning biomass pellets was accurately measured by using phosphor thermometry. The volatile gas temperature was measured using two-line atomic fluorescence thermometry. PAH emission was monitored using two-dimensional laser-induced fluorescence.

W. Weng and H. Feuk planned the experiment, and I conducted all the measurements together with W. Weng and H. Feuk. W. Weng is responsible for setting up the burner, flames, two-atomic fluorescence thermometry, and PAH PLIF measurement to which I also contribute. H. Feuk is responsible for surface temperature measured by using phosphor thermometry. I also contribute to analyzing the TLAF and PLIF datasets and improving the manuscript, reviewing, and editing.

Paper III: Quantitative imaging of potassium release from single burning pulverized biomass char particles.

*W. Weng, **S. Li**, M. Costa, and Z. Li, Fuel 264 (2020) 116866.*

In this paper, the release of potassium from single burning pulverized wheat straw char particles was quantitatively measured using laser-induced photofragmentation fluorescence (LIPF) with sizes in the range 224–250 μm. The potassium hydroxide (KOH) distribution surrounding the burning char particle was determined. The results show that the potassium release rate is almost constant of 0.5 μg/s during the char oxidation process from 10 to 70 ms, and that KOH represents over 60% of the total potassium. The results indicate that the LIPF imaging method can be used to study the potassium release from burning biomass fuels.

W. Weng planned the experiments, and I conducted all the measurements together with W. Weng. The biomass char powder was provided by M. Costa. I conduct data curation and analysis. I also contribute to improving the manuscript, reviewing, and editing.

Paper IV: Particle temperature and potassium release during combustion of single pulverized biomass char particles.

*W. Weng, **S. Li**, M. Costa, Z. Li, Proceedings of the Combustion Institute 38 (2021) 3949-3958.*

In this paper, we investigated the combustion characteristics of single pulverized biomass-derived char particles from wheat straw, grape pomace, kiwi branches and rice husk. The char particles were injected upward into a confined region of hot combustion products produced by flat flames stabilized on a McKenna burner, with mean temperatures of 1460, 1580 and 1670 K and mean O_2 concentrations of 4.5, 6.5 and 8.5 vol%. The particle temperature was obtained through two-color pyrometry technique. The potassium release rate was measured using a laser-induced photofragmentation fluorescence imaging technique. Particle ignition delay time and burning time, derived from the temporal evolution of the thermal radiation intensity of the burning char particles, have also been investigated.

W. Weng and I planned the experiment and conducted all the measurements together. W. Weng is responsible for setting up the burner, flames, lasers and performing temperature measurements using two-color thermometry to which I also contribute. I am responsible for the potassium release rate measurement by using LIPF technique. I also contribute to analyzing the particle combustion characteristic and the improvement of the manuscript, reviewing, and editing.

Paper V: Clustering-based particle detection method for digital holography to detect the three-dimensional location and in-plane size of particles

*J. Huang, **<u>S. Li</u>**, Y. Zi, Y. Qian, W. Cai, M. Aldén, Z. Li, Measurement Science and Technology 32 (2021) 055205.*

In this work, a new clustering-based particle detection (CBPD) method was proposed for digital holography based on clustering algorithms. The results of both simulations and experiments confirmed the feasibility of our proposed method. Without any manual thresholds, this data-driven method features automatic recognition of particles, particle edges and background, and accurate separation of overlapping particles.

I and J. Huang initiated the idea and planned all the measurements. Others contribute to improving the manuscript.

Paper VI: Quantification of the size. 3D location and velocity of burning iron particles in premixed methane flames using high-speed digital in-line holography

*J. Huang†, **<u>S. Li</u>**†, W. Cai, Y. Qian, E. Berrocal, M. Aldén, Z. Li, Combustion and Flame 230 (2021) 111430.*

In this paper, high-speed digital in-line holography (DIH) is employed to reconstruct the 3D particle field and simultaneously quantify the size, 3D location and velocity of burning iron particles. The statistical results of three iron dust flames with oxygen volume fractions varying from 24% to 40% are obtained and compared at different heights above the burner.

I and J. Huang initiated the idea and planned all the measurements. Others contribute to improving the manuscript.

Paper VII: A versatile metal powder burner for quantitative optical diagnostics of single burning particles and percolation flames.

***<u>S. Li</u>**, J. Huang, W. Weng, Y. Qian, M. Aldén, Z. Li, In Manuscript.*

In this work, a micron-size metal powder sieving and supplying set-up has been designed. The apparatus is based on two electrodes, which are connected to high

DC voltage as a high voltage capacitor (oscillator). It can fluidize the conductive powder between two electrodes. This dispersion system is well calibrated for the seeding concentration for different size iron particles using real-time weight measurements with external high voltage till up 20 KV. This supplying system can provide a stable flow of particle seeding for about one minute, which is of importance for quantity optical measurement. The particle velocity in the gas flow has been identified through high-speed shadowgraph imaging and particle tracking velocimetry (PTV). Stable combustion flame of iron, aluminum, and biomass char powder have been demonstrated. FeO, AlO, and alkali emission spectrum were identified.

I initiated the idea to design this burner from discussion with Zhongshan Li. I and Y. Qian fulfilled the drawing and design. I planned and conducted all the measurements. I evaluated experimental data and wrote the manuscript. Others contribute to improving the manuscript.

Paper VIII: Ignition and combustion behavior of single micro-size iron particle in hot gas flow.

*<u>**S. Li**</u>, J. Huang, W. Weng, Y. Qian, X. Lu, M. Aldén, Z. Li, Combustion and Flame 241 (2022) 112099.*

In this paper, the ignition and combustion process characteristics of burning different single micro-size iron particles have been investigated. It turns out that the particle size and combust product oxygen concentration are two key factors that affect the ignition and combustion properties of burning iron particles. Several distinct stages were observed and defined in the process of ignition and combustion. Particle temperatures are measured by two-color pyrometer technique. An important phenomenon of releasing during the iron particle burning process has been identified for the first time. In addition, the microstructure of raw and burnt iron particles were analyzed by scanning electron microscopy. The observed luminous release process was images of thermal radiation of the formed iron-oxide nanoparticles.

I initiated the idea and planned all the measurements. I conducted all the experiments. I and J. Huang extracted experimental data. I did the data analysis and wrote the manuscript. Others contribute to improving the manuscript.

Paper IX: A detailed study on the micro-explosion of burning iron particles in hot oxidizing environments.

*J. Huang†, <u>**S. Li**</u>†, D. Sanned, L. Xu, S. Xu, Y. Qian, Q. Wang, M. Stiti, W. Cai, E. Berrocal, M. Aldén, M. Richter, Z. Li, Combustion and Flame 230 (2021) 111430.*

In this paper, the micro-explosion behavior of burning iron particles was experimentally investigated based on advanced optical diagnostics. The three-dimensional (3D) motion and mean surface temperature of burning iron particles during the micro-explosion process were measured using the stereo imaging technique and two-color pyrometry, respectively. The probability of micro-explosions in different oxidizing environments was statistically studied. Three distinct micro-explosion modes have been observed. The results showed that the micro-explosion of burning iron particles heavily depended on oxygen concentration. Three types of potential gas sources inside the particle were discussed regarding the mechanism of the micro-explosion. The sharp gradients of gas temperature and oxygen concentration may facilitate the rapid increase of the internal pressure in the particle, which eventually causes the micro-explosion.

I and D. Sanned initiated the idea and planned all the measurements. I, D. Sanned, E. Berrocal, and *J. Huang conducted all the experiments. L. Xu and S. Xu did the simulation. I, D. Sanned, and J. Huang evaluated and analyzed all the experimental data and wrote the manuscript. Others contribute to improving the manuscript.*

Paper X: Stereo High-Speed imaging of iron particles micro-explosions and nanoparticles-release.

__S. Li__, D. Sanned, J. Huang, E. Berrocal, W. Cai, M. Aldén, M. Richter, Z. Li, Optics Express, 21 (2021) 34465-34476.

In this paper, the combustion regimes of iron particles ($d = 80$ μm) in a laminar diffusion flame are detailed studied during lean diffusive flame conditions with surrounding oxygen concentration of around 39%. The 3D-velocity measurements of burning iron particles have been performed with two high speed cameras in stereo configuration. The results of particle temperature evaluation in the combustion zone together with quantitative observations of single burning iron particles through high-speed imaging are presented. Particles are observed to change the direction of their trajectories after violent explosions into smaller pieces that quickly burn out. The iron particle explosion is an important process, especially for industrial applications of iron combustion since it can affect both combustion stability and the formation of product components. Another critical phenomenon was observed and further studied using shadowgraphy for the first time, namely the release of nanoparticles during the iron particle burning process.

I and D. Sanned initiated the idea and planned all the measurements. I, D. Sanned and E. Berrocal conducted all the experiments. D. Sanned and I evaluated and analyzed all the experimental data and wrote the manuscript. Others contribute to improving the manuscript.

Paper XI: Phase change and combustion of iron particles in premixed CH$_4$/O$_2$/N$_2$ flames.

*S. Xu, Y. Qiu, L. Xu, <u>**S. Li**</u>, E.J.K. Nilsson, Z. Li, M. Aldén, X-S Bai, Submitted to Combustion and Flame.*

Metal powder is a promising carbon-free and recyclable energy carrier. Direct combustion of micron-sized iron particles involves complex physical and chemical processes, such as heat transfer, surface reaction, and phase change. In this work, computational modelling of these processes are investigated and validated against experiments. A single iron particle combustion and phase change model is proposed in an Eulerian-Lagrangian framework. The new model considers five stages, i.e., solid-phase oxidation, melting of iron oxides and raw iron, liquid-phase oxidation, cooling of liquid iron oxides, and solidifying supercooled liquid iron oxides. The proposed model is first validated and then adopted in micron-sized iron particle combustion simulations in premixed CH$_4$/O$_2$/N$_2$ flames to study the effects of ambient temperature and oxygen concentration on single iron combustion.

Y. Qiu and S. Xu initiated the idea and planned all the simulations, writing, analyzing and finalizing the paper. I provided all experimental results to fit kinetic modeling and CFD simulation and contribute to the results discussions.

Division of Combustion Physics
Department of Physics

LUND
UNIVERSITY